

CRYOSMOS

WP500

Case Studies: Retrieval Methodology Development
and Validation

D5-2 Algorithm Theoretical Basis Documents (ATBD) v2

Version 1.0
November 9, 2016



This page is intentionally left blank

ESA STUDY CONTRACT REPORT			
ESRIN CONTRACT NO: 4000112262/14/I-NB	SUBJECT: CryoSMOS Support To Science Elements SMOS+Cryosphere	CONTRACTOR: IFAC	
ESA CR ()No:	STAR CODE:	No of volumes: 1 This is volume no: 1	CONTRACTOR'S REF: Deliverable D5-2
<p>ABSTRACT:</p> <p>This is part of the Task 4 activity of the project (Deliverable D5-2) <i>CryoSMOS - Support To Science Elements SMOS+Cryosphere</i> (ESRIN Contract No. 4000112262/14/I-NB). It contains the detailed description of the final methods and algorithms on the basis of the previous detailed experimental analysis that will be used for the retrieval of the physical parameter.</p>			
<p>The work described in this report was done under ESA Contract. Responsibility for the contents resides in the author or organisation that prepared it.</p>			
<p>PREPARED BY: G. Macelloni, F. Montomoli, M. Brogioni, (IFAC), N. Skou, R. Forsberg (DTU), M. Leduc-Leballeur, G. Picard (LGGE), L. Kaleschke, A. Wernecke (UHAM), A. Mialon (CESBIO)</p>			
ESA STUDY MANAGER: Ola Grabak		ESA BUDGET HEADING	

This page is intentionally left blank

DOCUMENT CHANGE LOG

Issue/ Revision	Date	Observations
1/0	07/11/2016	First issue

This page is intentionally left blank

Table of Contents

1 Purpose and structure of document	9
1.1 Purpose	9
1.2 Document Structure	9
1.3 Definitions and Acronyms.....	10
1.4 Reference documents.....	11
2 Case study n.1: quantifying internal ice-sheet temperature	13
2.1 Brief description	13
2.2 Temperature Profile: Retrieval Approach – Final ATBD	14
2.2.1 Data description	14
2.2.2 Ice sheet temperature model.....	15
2.2.3 The electromagnetic model	16
2.2.4 The algorithm	20
2.2.5 Retrieval Products	27
3 Case study n.2: bedrock topography and/or geothermal heat flux	31
3.1 Brief Description of the Case Study	31
3.2 Correction for -10 m Physical Temperature.....	33
3.3 DomeC ice thickness estimation.....	40
3.4 East Antarctica ice thickness estimation from SMOS data.....	42
4 Case study n.3: characterization of ice shelves.....	53
4.1 Brief description of the case study	53
4.2 Characterization of the ice shelves: Retrieval Approach or Methodology – Final ATBD	53
4.2.1 The Emission Model	53

4.2.2	SMOS data	55
4.2.3	Method	58
4.2.4	Sensitivities	60
4.2.5	A brief Overview	61
5	Case study n.4: characterization of surface processes	63
5.1	Brief description of the case study	63
5.2	Characterization of surface processes: Retrieval Approach or Methodology – Final ATBD	64
5.2.1	SMOS observation selection process	64
5.2.2	The algorithm	64
5.2.3	Final product.....	65
6	References	67

1 Purpose and structure of document

1.1 Purpose

This document contains the description of the final method and algorithms that will be used to generate the prototypal SMOS-based products for each case study.

1.2 Document Structure

The structure of the document is the following (and summarized in Table 1-1 against WPs):

- Section 2 – 5 Detailed description of the final Algorithm Theoretical Basis Documents (ATBD) for each case study.
- Section 6 – References.

Table 1-1 - Structure of document against subtasks of the work package

WP	Subtask	Section(s) in document	Main contributors
500	1	2	IFAC
500	2	3	DTU
500	3	4	UH
500	4	5	LGGE

1.3 Definitions and Acronyms

Table 1-2 lists the acronyms and abbreviations used within this document.

Table 1-2 - Acronyms and abbreviations

Acronym	Meaning
AMSR-E	Advanced Microwave Scanning Radiometer for EO
AMSR-2	Advanced Microwave Scanning Radiometer
AMSU	Advanced Microwave Sounding Unit
CEOS-WGCV	Committee on Earth Observation Satellites-Working Group Calibration and Validation
CESBIO	Centre d'Etudes Spatiales de la BIOSphère
CSCR	Case Studies Consolidation Report
DMRT	Dense Media Radiative Transfer model
DTU	Danish Technical University
ECV	Essential Climate Variables
EM	ElectroMagnetic
EO	Earth Observation
EOEP	Earth Observation Envelope Program
EPICA	European Project for Ice Coring in Antarctica
ESA	European Space Agency
GOCE	Gravity field and steady-state Ocean Circulation Explorer
IFAC	Istituto di Fisica Applicata "N.Carrara"
IR	InfraRed
ITT	Invitation To Tender
LGGE	Laboratoire de Glaciologie et Géophysique de l'Environnement
MODIS	Moderate Resolution Imaging Spectroradiometer
MIRAS	Microwave Imaging Radiometer by Aperture Synthesis
ML	Multi-Layer
NIR	Noise Injection Radiometers
NASA	National Aeronautics and Space Administration

QCA-CP	Quasi Crystalline Approximation with Coherent Potential
RB	Requirement Baseline report
SMAP	Soil Moisture Active and Passive mission
SMOS	Soil Moisture Ocean Salinity mission
SoW	Statement Of Work
SSM/I	Special Sensor Microwave Imager
STSE	Support To Science Elements
TB	Brightness Temperature
UHAM	University of Hamburg
WALOMIS	Wave Approach for LOw-frequency Mlcrowave emission in Snow
WP	Work Package

1.4 Reference documents

All the references to scientific works cited in the present report are reported in section 6. Hereinafter are listed some general management documents referred in the present report:

[RD.1] Project Statement of Works

[RD.2] CryoSMOS project proposal

[RD.3] D1 - Requirement Baseline report (RB)

[RD.4] D2 - Case Studies Consolidation report (CSC)

[RD.5] D3 - Dataset

[RD.6] D4 - Dataset User Manual (DUM)

[RD.7] D5-1 - Algorithm Theoretical Basis Documents (ATBD) v1

[RD.8] D6-1 - Product Validation Report (VR) v1

This page is intentionally left blank

2 Case study n.1: quantifying internal ice-sheet temperature

(IFAC-CNR in cooperation with LGGE, CESBIO)

2.1 Brief description

The present case study deals with the estimation of the ice sheet temperature profile by using SMOS data. In deliverables D2 (Case Study Consolidation Report) has been pointed out in details how the brightness temperature of the Antarctic plateau is linked to the ice cap parameters. The T_b depends on the ice sheet permittivity ε and the ice temperature profile that, in the most stable regions of the plateau, can be described by the Robin model (Robin, 1955) whose main driving parameters are the surface temperature (T_s), the ice thickness (H), the geothermal heat flux (G) and the snow mean accumulation (M)

$$T_b = f(T(z), \varepsilon(z)) \quad (2.1)$$

$$T(z) = T_s + \frac{G}{2\sqrt{\frac{M c \rho}{2HK}}} \sqrt{\pi} \left(\operatorname{erf} \left[z \sqrt{\frac{M c \rho}{2HK}} \right] - \operatorname{erf} \left[H \sqrt{\frac{M c \rho}{2HK}} \right] \right) \quad (2.2)$$

In (2.2) z is the vertical coordinate upward with the origin at the ice-bed interface, c is the specific heat capacity ($45 \text{ m}^2/\text{yr}$), K is the ice thermal conductivity ($2.7 \text{ W/m}^2 \text{ K}^{-1}$) and ρ is the average density profile.

From (2.1) and (2.2) it is evident that for the retrieval of the ice temperature profile from T_b measurements collected by SMOS additional information on the geophysical parameters governing the temperature profile is needed.

Surface temperature can be obtained from several sources. In the present algorithm data from a glaciological model were used. Also, ice thickness can be obtained from detailed ground measurements that were collected almost all over Antarctica. These two kinds of data are available to the community with enough accuracy and can be used directly in the retrieval algorithm. Moreover, the impact of an error on these parameters is considered in deliverable [D6-2]. Also geothermal heat flux and snow accumulation are estimated over the continent by glaciological models, however they have more uncertainty than T_s and H . The algorithm developed here is based on the minimization of a cost function with respect to the two geophysical parameters which have a great uncertainty: G and M . Data available in literature are used as first guess in the retrieval. For sake of convenience it will be referred to T_s and H as “ancillary data” and to G and M as “a-priori information” in the rest of document. The ice temperature profile is estimated by simulating the SMOS measurements with an electromagnetic emission model whose inputs are in part fixed for each pixel (auxiliary data) and some are let varying in a given range around the a-priori information. The pair of (G, M) that allows the best simulation of SMOS data will then be used with the auxiliary data to derive the ice temperature profile by using Robin model.

2.2 Temperature Profile: Retrieval Approach – Final ATBD

2.2.1 Data description

The method adopted for the retrieval of the ice sheet temperature profile uses different kind of input data, namely SMOS data, ancillary and a-priori parameters.

The main inputs of the algorithm are SMOS L3 v300 data collected over Antarctica and monthly or annually averaged. This data are produced by CATDS (Centre Aval de Traitements des Données SMOS) by processing SMOS L1C data and reprojecting them over the EASE2 grid. The data essentially consist of brightness temperature measurements at V and H polarizations averaged every 5 degrees in the angular pattern in the range 2.5 deg to 62.5 deg (D4 – Dataset User Manual).

Auxiliary information is inferred from ancillary data and a-priori parameters from different sources namely:

Ancillary parameters

- Mean surface temperature map (T_s). Temperature data are obtained by using the CROCUS model (Freville *et al.*, 2013) and provided to the consortium by LGGE.
- Ice thickness map (H). Obtained from the “Thickness” dataset of the Bedmap2 database (Fretwell *et al.*, 2016). Data available at <https://www.bas.ac.uk/project/bedmap-2/>

A-priori parameters

- Geothermal Heat Flux (G). This kind of data (described in Fox Maule *et al.*, 2005) is a subset of the ALBMAP database (Le Brocq *et al.*, 2010). ALBMAP can be downloaded from <https://doi.pangaea.de/10.1594/PANGAEA.734145>
- Snow accumulation map (M). Data are provided by LGGE according to (Agosta *et al.*, 2013) obtained using the RACMO model (Regional Atmospheric Climate Model).

SMOS and auxiliary data are geocoded and co-registered over the EASE2 grid by CESBIO in order to have a consistent database to produce the internal ice sheet temperature maps.

In Figure 2-1 are represented the auxiliary datasets used as input to the retrieval algorithm. For easiness of representation the data were reprojected in polar stereographic coordinates. Also, the level lines are represented in gray.

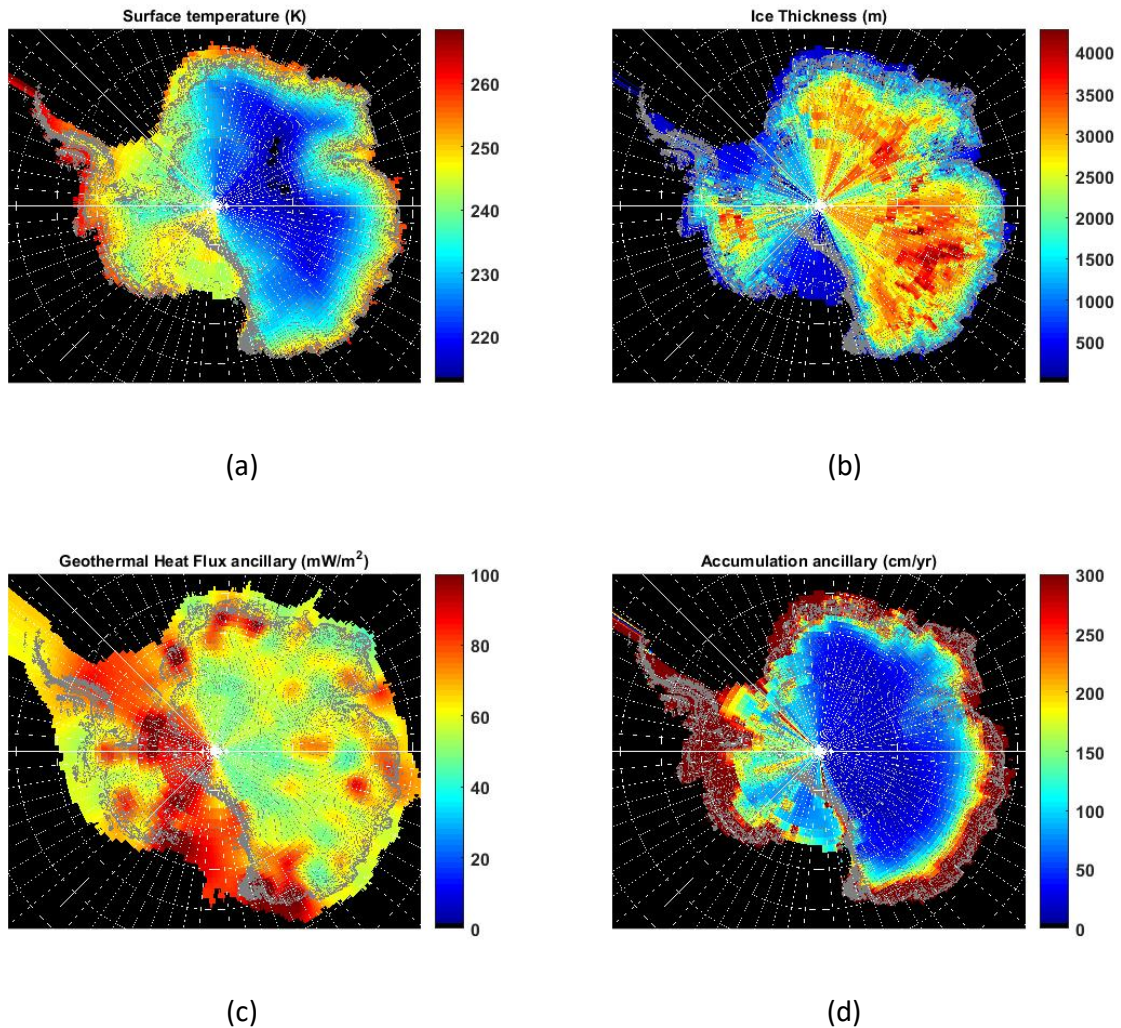


Figure 2-1: The auxiliary data used in the retrieval algorithm: surface temperature T_s (a), ice thickness H (b), geothermal heat flux G (c) and snow accumulation M (d). For sake of convenience the datasets have been represented reprojected in polar stereographic coordinates.

2.2.2 Ice sheet temperature model

A glaciological model is used to provide estimates of the temperature profile of the ice sheets. The selected one is the Robin model (Robin et al., 1955), summarized in equation 2.2 and described in detail in [D5-1]. Thermal conductivity and diffusivity of ice are assumed constant, fixed at $2.7 \text{ W/m}^2 \text{ K}^{-1}$, and $45 \text{ m}^2/\text{year}$ respectively.

This model is used to estimate the ice temperature of those regions characterized by a negligible horizontal advection. These regions are essentially the ones which experienced a very slow horizontal movements and are mainly located in the internal part of the East Antarctic Plateau. In order to select the areas of ice sheets where Robin model can be applied we used the surface mass balance velocity

map produced by (Bamber *et al.*, 2000). The map is freely available online at http://websrv.cs.umd.edu/isis/index.php/Present_Day_Antarctica. A threshold of 5 m/year of the surface balance velocity was set to find the Robin model validity regions. Indeed, above this value the horizontal advection cannot be considered negligible. Using this threshold, a map of Antarctica where the Robin model can be applied thus the ice temperature estimation is feasible has been generated (Figure 2-2). In order to consider a wider region of Antarctica, areas presenting a velocity between 5 and 10 m/year are also considered in the following chapters. In this case the expected quality of delivered product has been reduced.

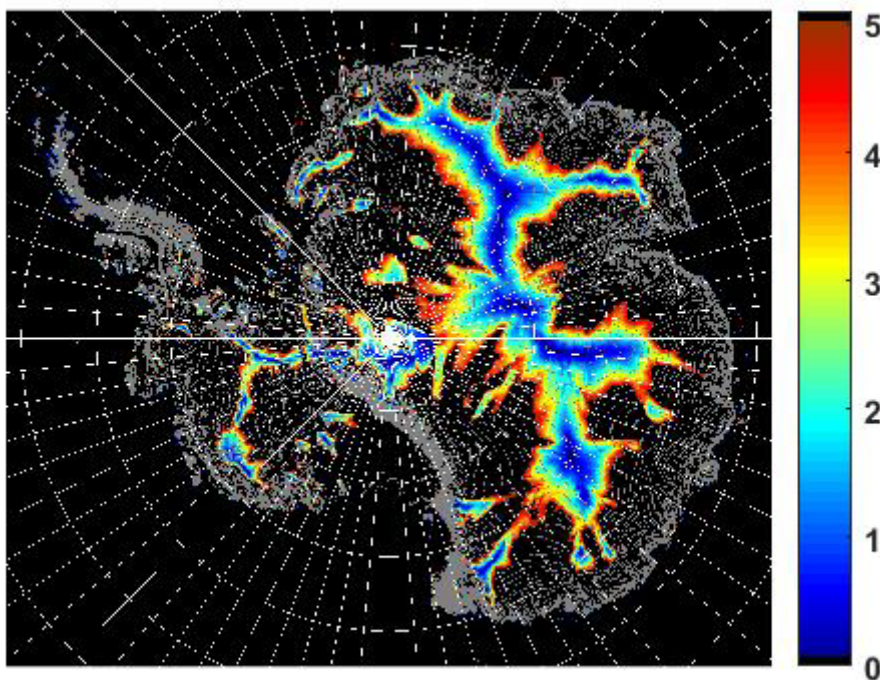


Figure 2-2: Mask of validity of the Robin Model (yellow areas). The map highlights those regions with a surface balance velocity lower than 5 m/yr, thus having a negligible lateral advection.

2.2.3 The electromagnetic model

The microwave emission model used to simulate the L-band SMOS data is WALOMIS (Wave Approach for LOW frequency Microwave emission in Snow) (Leduc-Leballeur *et al.*, 2015) a coherent electromagnetic model based on both West *et al.* (1996) and Tsang *et al.* (2000).

The modeled structure of the medium is multi-layered, with each layer characterized by its thickness, temperature, and density. In addition, in this case, scattering by snow grains is disregarded. Because of the use of the wave approach, the simulations obtained for a specific snowpack configuration (i.e. a given set of inputs) may differ considerably from those obtained using a slightly different snowpack. This

result is due to the high sensitivity of interference phenomena to layer optical depth. To take into account the variable nature of the snowpack in reality at a scale of one pixel and the finite aperture size of the antenna as well as of the bandwidth, it is essential to average a large number of simulations, using inputs that represent natural variability. A stochastic model is used to generate such profiles (examples in West et al., 1996, or in Leduc-Leballeur et al., 2015). The output of the model is the average of TB computed by using all the generated profiles.

An important part of the em model is the ice permittivity model. According to the work carried out in (Macelloni *et al.*, 2016). The more suitable model for simulating the spatial features of the SMOS measurements is the one proposed in Mätzler (2006) valid for the microwave range (1–200 GHz). The ice imaginary part predicted has a magnitude typically 10^{-4} at 1 GHz and -20 °C and is expressed by:

$$\varepsilon''_{ICE} = \left(\frac{a}{f} + b f \right) \quad (2.3)$$

$$a = (5.04 * 10^{-3} + 6.2 * 10^{-3} \theta) e^{-22.1 \theta} \quad (2.4)$$

$$b = \frac{2.07 * 10^{-2}}{T} \frac{e^{335/T}}{(e^{335/T} - 1)^2} + 1.16 * 10^{-11} f^2 + e^{-10.02 + 0.0364 (T - 273)} \quad (2.5)$$

$$\theta = \frac{300}{T} - 1 \quad (2.6)$$

Where f = frequency in GHz and T is ice temperature in Kelvins.

Still in (Macelloni *et al.*, 2016) it was highlighted that the use of the Mätzler model leads to an overestimation of the SMOS brightness temperature that can be corrected by imposing a bias in the model's simulations.

In order to properly determine such a bias, a specific analysis has been carried out for the sites of Dome C (DC) and Vostok Lake (VL), since in this areas the ice temperature profile was measured in the past. Specifically, it was compared the T_b simulated by WALOMIS to the SMOS data at V polarization in the incidence angular range of 32.5 - 62.5 deg. V polarization was chosen because it is less affected by the density fluctuations of the ice sheet. The T_b difference between modeled and simulated data is shown in Figure 2-3.

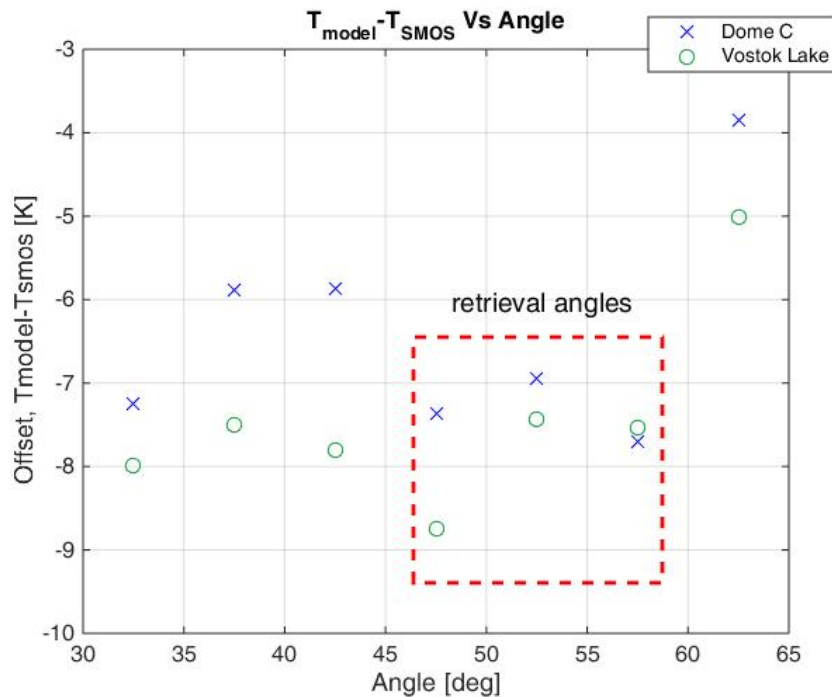


Figure 2-3: Difference between TbV calculated using Walomis and SMOS data, for Dome C (blue crosses) and Vostok Lake (green circles).

Figure 2-3 points out that the offset value is dependent on the incidence angle considered and it is not the same for DC and VS because of the different density profiles of the two sites. The offset values obtained are similar for angles closer to Brewster one since in this configuration the effects of density profile fluctuations on Tb are minimum. In order to find the optimal bias value for the best fitting, root mean square error between corrected modeled and measured Tb as a function of the offset was calculated and shown in Figure 2-4. Four cases were considered: RMSE computed with Tb in the range 32.5-57.5 deg incidence angle (a), 47.5-57.5 deg (b), 52.5-57.5 deg (c), 52.5 deg (d).

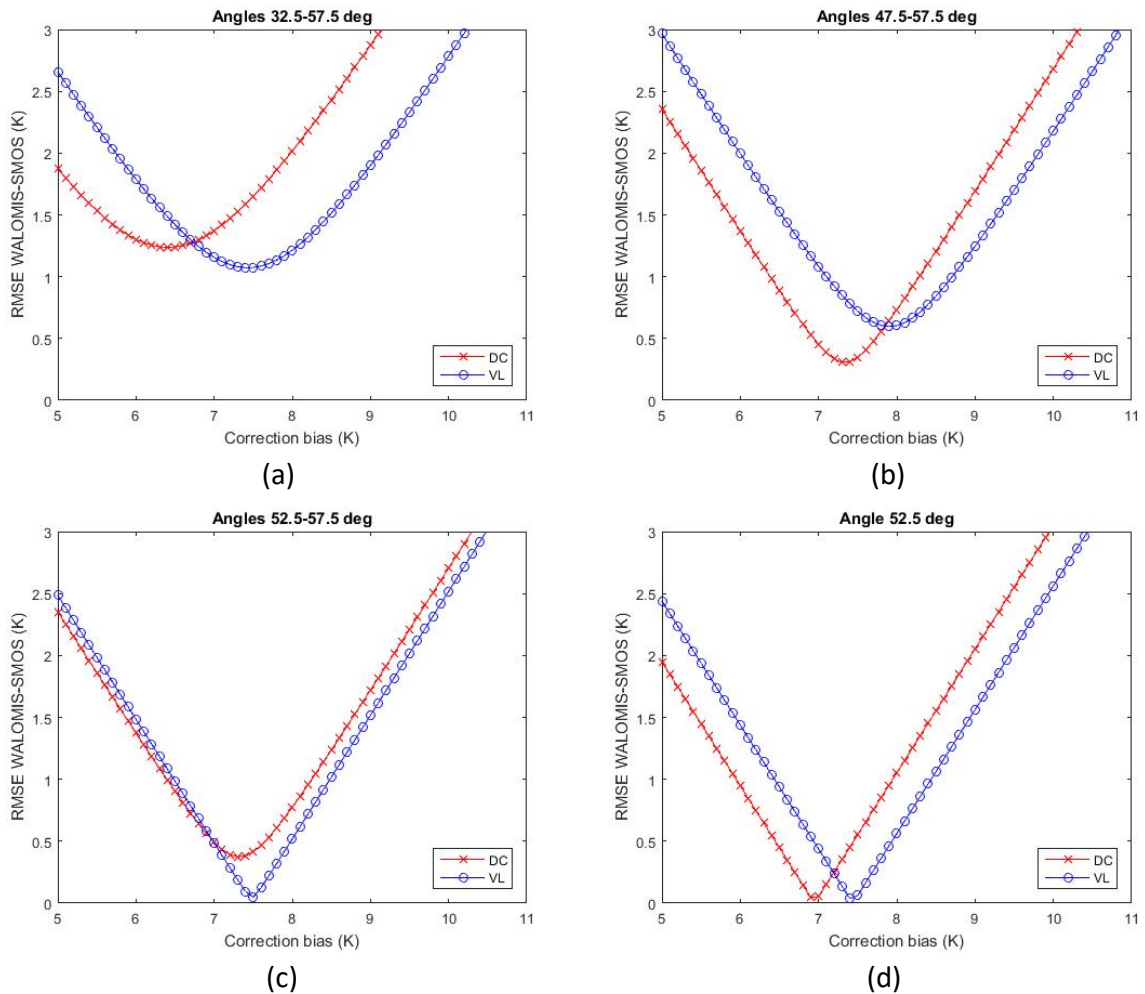


Figure 2-4: RMSE as a function of the offset for DC and VS test sites. The RMSE is computed between WALOMIS and SMOS data at V-pol for the angles ranges 32.5-57.5 deg (a), 47.5-57.5 deg (b), 52.5-57.5 deg (c), 52.5 deg (d).

The optimal value for the offset is dependent on the number of angles considered and is computed as the mean between the biases that produce minimum RMSE at DC and VS. In Table 2-1 are reported the values of the optimal offset for each range of angles considered. These values will be used in the next section during the selection of the most suitable configuration of the Cost Function in order to correct WALOMIS Tb simulations. As an example, a comparison of the Tb angular pattern before and after the correction is represented in Figure 2-5 with the bias of the 47.5-57.5 deg incidence angle range.

Table 2-1 – Optimal values of bias for the model fitting

	Incidence angle range (deg)			
	32.5-57.5	47.5-57.5	52.5-57.5	52.5
Optimal offset (K)	6.9	7.6	7.4	7.15

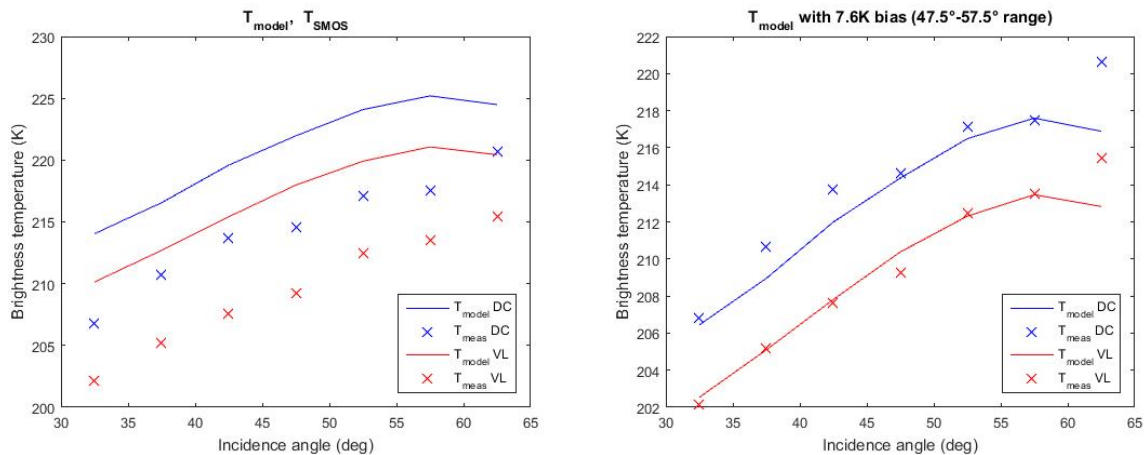


Figure 2-5: Brightness temperature as a function of observation angles for DC and VS before (left) and after the offset correction (right).

2.2.4 The algorithm

The algorithm is based on the minimization of a cost function whose kernel is the mean square error between the SMOS L3 measurements and the brightness temperature simulated by the WALOMIS model. In addition, a regularization function which accounts for the variability of the physical parameters to be retrieved is included. All of the main point of the cost function will be described in detail in the next sub-sections.

For each SMOS pixel, iterations are performed over the two free variables (i.e. the geothermal heat flux and the annual snow accumulation) which can vary around the first guess, was obtained from the a-priori information. as previously described (sect. 2.2.1). The cost function is computed for every allowed pair of G and M , then the minimum is determined and the associated optimal pair (G_{opt} , M_{opt}), i.e. the pair that makes the simulated T_b to minimize the cost function, selected for the ice sheet profile estimation. Finally, the glaciological model is run again to calculate the retrieved temperature profile using as inputs T_s , H , G_{opt} and M_{opt} .

Hereinafter are detailed the several steps of the retrieval procedure.

2.2.4.1 Pre-processing of input data

The entry point of the retrieval algorithm is the pre-processing of the input data. It is worth to recall that they come already re-projected and co-registered on the EASE2 grid in order to make easier the retrieval.

The first step of the pre-processing is the elimination from the five input maps (T_b V pol, T_s , IT , G and M) of all of those pixel that lies outside the Robin model validity mask (see Figure 2-2). Also, since the

sensitivity of Tb to the ice thickness is on the order of 1K per 300-500 m of ice thickness, all of the areas whose ice thickness is lower than 1000 m were disregarded since the error on the SMOS measurements is on the same order of the ice sheet emitted Tb.

Then the SMOS L3 data are temporally averaged in order to have a brightness temperature map representative of the emission over a long time period. It is expected that the Tb at L-band cannot have appreciable temporal variations, thus all of those pixel with a temporal standard deviation greater than 1 K were disregarded.

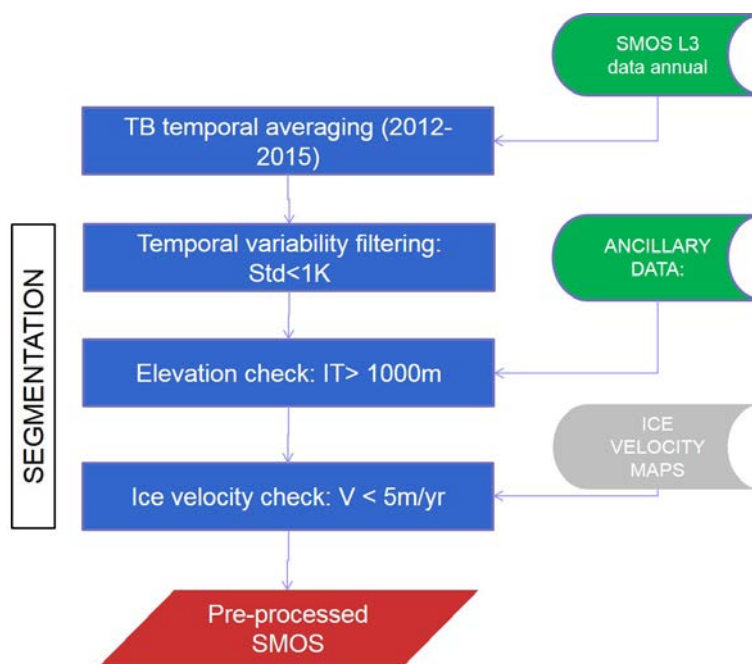


Figure 2-6: Pre-processing of SMOS L3 data

After having spatially filtered the input datasets and also temporally averaged the SMOS measurements, the pre-processing is concluded and all of the data are ready to be used in the retrieval algorithm.

In Figure 2-7 are shown the regions over which the ice sheet temperature profile retrieval will be performed. The threshold applied were: standard deviation of Tb at V polarization lower than 1 K, ice thickness higher than 1000 m, surface balance velocity lower than 5m/yr (green) and between 5 and 10 m/yr (blue). Robin model strictly applied in green regions, however the retrieval is performed also in blue area with a lower confidence. Every pixel is marked with a specific confidence flag to reflect these two conditions.

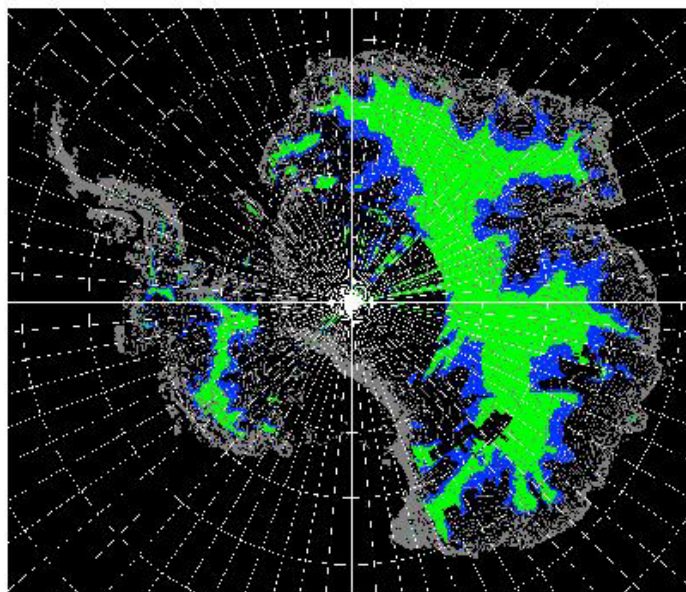


Figure 2-7: Mask of applicability of the ice sheet temperature profile retrieval. The green and blue areas indicate surface balance mass velocity lower than 5m/yr and between 5 and 10 m/yr respectively, standard deviation of TbV lower than 1K, ice thickness higher than 1000m.

2.2.4.2 The retrieval procedure

The inversion procedure aims at determining for each pixel the optimum couple of G and M corresponding to the minimum of the cost function $CF(G, M)$ presented in the next section. The iteration runs for every value of G and M in the search interval around the a-priori parameter as for example $(G_{anc} \pm 50\%, M_{anc} \pm 20\%)$. Indeed, it is widely recognized that the uncertainty on the a-priori value is higher for G than M . The definition of the optimum interval is explained in section 2.2.4.4, as well as the determination of the incidence angles to be considered in the Cost Function.

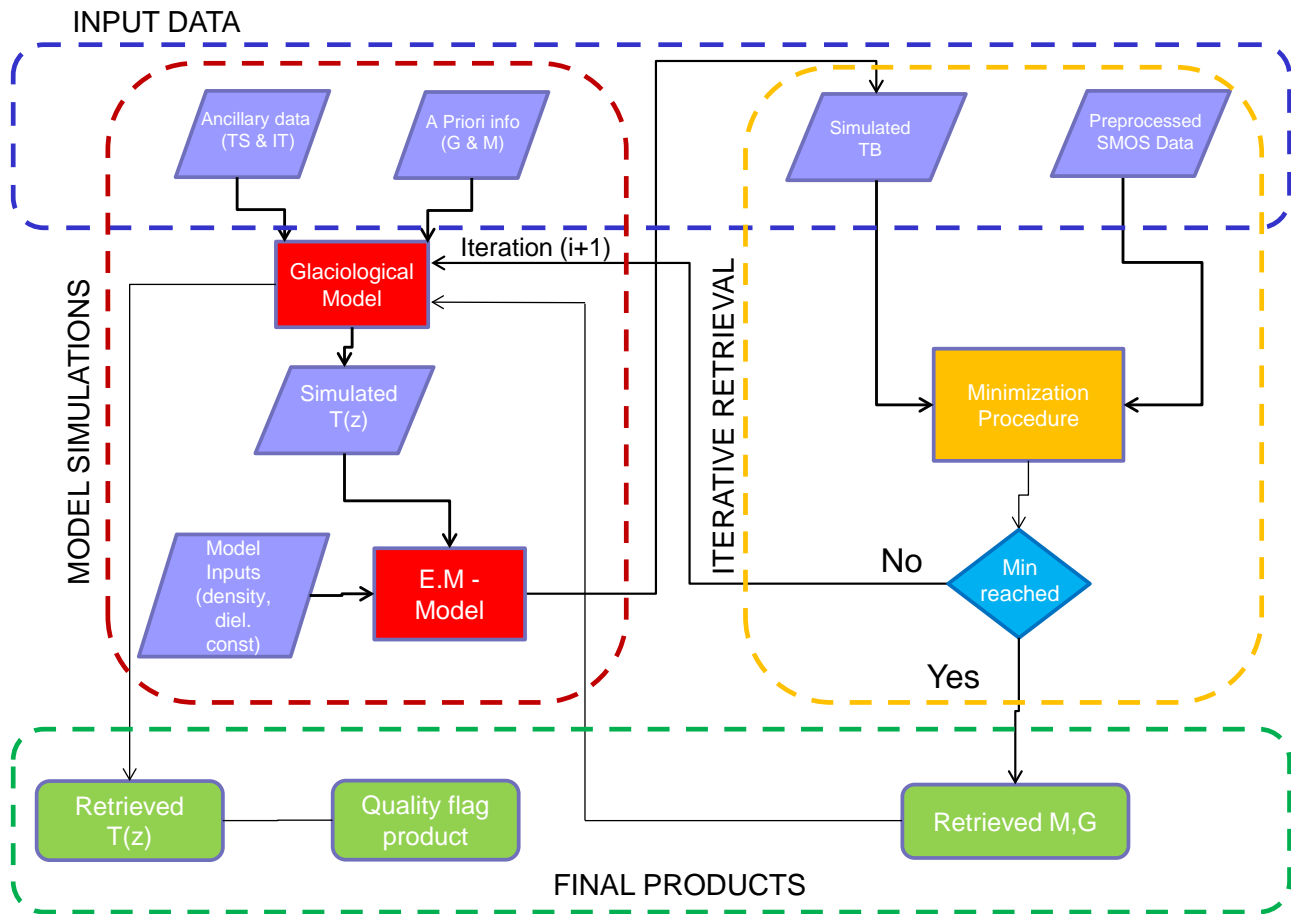


Figure 2-8: Flow chart of the retrieval algorithm

2.2.4.3 The Cost Function

For each observation angle, cost function is composed by the mean square error between the pre-processed SMOS angular data and the simulated TB plus a regularization part which Accounts for the a-priori information. Moreover, the variability of the different data is taken into account by normalizing each term by the standard deviation of the relative input. For each combination of (G, M) the CF is described as follows:

$$\begin{aligned}
 CF(G, M) = & \frac{1}{N_{\theta}} \frac{1}{\sigma_{TB}^2} \sum_{\theta=\theta_1}^{\theta_n} \|T_{b\ SMOS}(\theta) - T_{b\ WALOMIS}(\theta, G, M)\|^2 + \\
 & + \frac{1}{\sigma_G^2} \|G_{anc} - G\|^2 + \frac{1}{\sigma_M^2} \|M_{anc} - M\|^2
 \end{aligned} \tag{2.7}$$

where:

- $T_{b\ SMOS}(\theta), T_{b\ WALOMIS}$ are the measured and the simulated Tb for different angles of observation.
- G_{anc}, M_{anc} are the a-priori values
- $\sigma_{TB}, \sigma_G, \sigma_M$ are the standard deviation of SMOS data, geothermal heat flux and snow accumulation respectively. For SMOS σ_{TB} is calculated on Tb annual average.
- N_θ is the number of incidence angles considered in the retrieval.

The standard deviation of the input data uncertainties is summarized in Table 2-2. The standard deviation of the Tb was computed from the monthly averages of the L3 data, the uncertainty of geothermal heat flux was derived from (Fox Maule *et al.*, 2005), the one of the annual snow accumulation from (Agosta *et al.*, 2013).

Table 2-2 : Parameter's configuration in the Cost Function

σ_{TB}	σ_G	σ_M
0.15 K	0.024 mW/m ²	0.003 m/yr

2.2.4.4 Optimization of the Cost Function

Previous section 2.2.4.3 described the general structure of the Cost Function that is used in the retrieval. However, some important parameter of the CF cannot be imposed a-priori but should be tuned accordingly to the physical processes involved. For instance: the incidence angles to be considered in the computation of the RMSE, or if the regularization part should be considered or not. In order to setup properly the cost function, several configurations have been considered and tested over the transect from Dome C to Vostok Lake which was investigated in (Macelloni *et al.* 2016).

The parameters of the several configurations tested were:

- Number of angles over which computing the RMSE: 1, 2 or 3 angles close to Brewster one.
- Perform the retrieval for a single pixel or consider more consecutive pixels. In the latter case, a weight should be applied to the RMSE of these "extra-pixels" in the cost function calculation (equal weight, triangle weight i.e. the extra pixel has a cost doubled w.r.t. the one examined).
- A-priori search range for the basal heat flux G : a-priori value $\pm 30\%$, a-priori value $\pm 50\%$, a-priori value 70% . The search range of the accumulation M range was kept fixed at the a-priori value $\pm 20\%$ because it is widely recognized that the M values are much more reliable than G values model estimates.
- If to consider or not the regularization term in the Cost Function.

CRYSMOS

ESA contract No.4000112262/14/I-NB

For each configuration obtained by combining the previous cases, the retrieval of the ice sheet temperature profile was performed over the transect. Then, in order to evaluate the performance of each configuration, we considered the error of the estimates of G and M at DC and VL test sites, the RMSE and the mean bias between SMOS and WALOMIS simulations over the entire transect. In

Case	a-priori search range	Regularization	Near pixels	Weights	Case	a-priori search range	Regularization	Near pixels	Weights	Case	a-priori search range	Regularization	Near pixels	Weights
1	±30%	no	no	-	9	±50%	no	no	-	17	±70%	no	no	-
2	±30%	no	yes	1, 1, 1	10	±50%	no	yes	1, 1, 1	18	±70%	no	yes	1, 1, 1
3	±30%	no	yes	1.5, 1, 1.5	11	±50%	no	yes	1.5, 1, 1.5	19	±70%	no	yes	1.5, 1, 1.5
4	±30%	no	yes	2, 1, 2	12	±50%	no	yes	2, 1, 2	20	±70%	no	yes	2, 1, 2
5	±30%	yes	no	-	13	±50%	yes	no	-	21	±70%	yes	no	-
6	±30%	yes	yes	1, 1, 1	14	±50%	yes	yes	1, 1, 1	22	±70%	yes	yes	1, 1, 1
7	±30%	yes	yes	1.5, 1, 1.5	15	±50%	yes	yes	1.5, 1, 1.5	23	±70%	yes	yes	1.5, 1, 1.5
8	±30%	yes	yes	2, 1, 2	16	±50%	yes	yes	2, 1, 2	24	±70%	yes	yes	2, 1, 2

are reported the characteristics of each case considered. The results of the analysis are represented in Figure 2-9.

Table 2-3: The different cases for the configuration of the Cost Function

Case	a-priori search range	Regularization	Near pixels	Weights	Case	a-priori search range	Regularization	Near pixels	Weights	Case	a-priori search range	Regularization	Near pixels	Weights
1	±30%	no	no	-	9	±50%	no	no	-	17	±70%	no	no	-
2	±30%	no	yes	1, 1, 1	10	±50%	no	yes	1, 1, 1	18	±70%	no	yes	1, 1, 1
3	±30%	no	yes	1.5, 1, 1.5	11	±50%	no	yes	1.5, 1, 1.5	19	±70%	no	yes	1.5, 1, 1.5
4	±30%	no	yes	2, 1, 2	12	±50%	no	yes	2, 1, 2	20	±70%	no	yes	2, 1, 2
5	±30%	yes	no	-	13	±50%	yes	no	-	21	±70%	yes	no	-
6	±30%	yes	yes	1, 1, 1	14	±50%	yes	yes	1, 1, 1	22	±70%	yes	yes	1, 1, 1
7	±30%	yes	yes	1.5, 1, 1.5	15	±50%	yes	yes	1.5, 1, 1.5	23	±70%	yes	yes	1.5, 1, 1.5
8	±30%	yes	yes	2, 1, 2	16	±50%	yes	yes	2, 1, 2	24	±70%	yes	yes	2, 1, 2

CRYOSMOS

ESA contract No.4000112262/14/I-NB

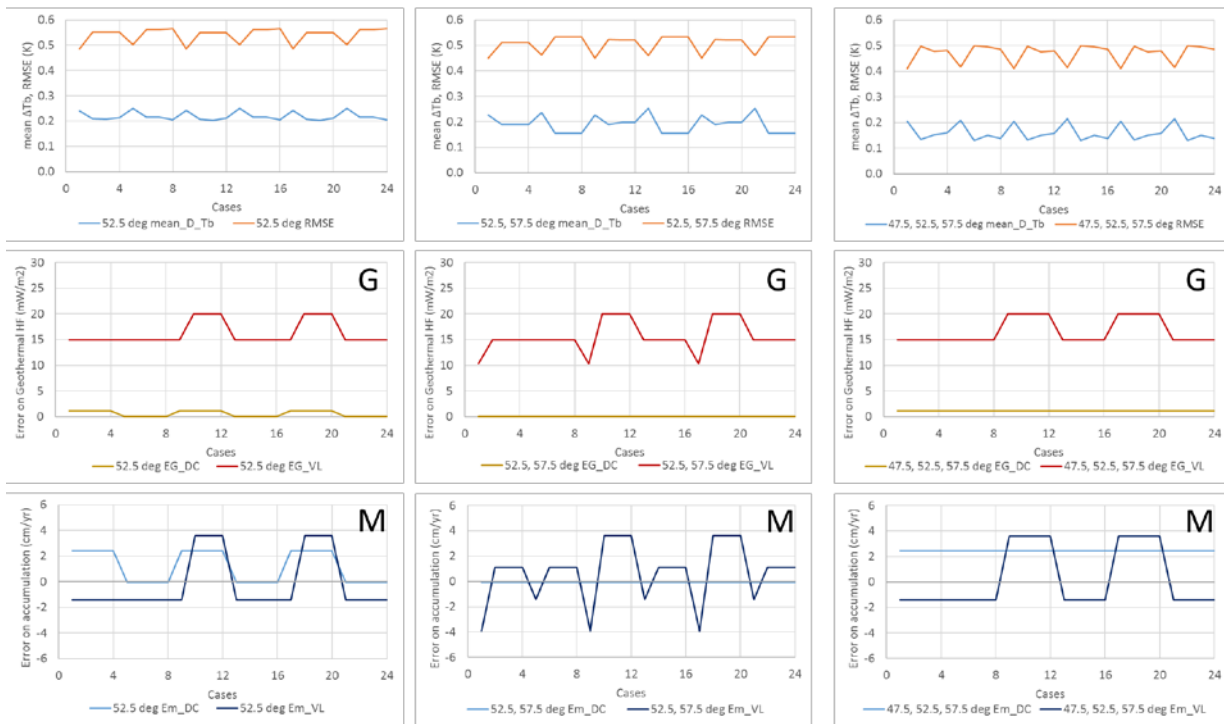


Figure 2-9: Performances of the Cost Function for the several configuration considered. The characteristics of the cases are reported in

Case	a-priori search range	Regularization	Near pixels	Weights	Case	a-priori search range	Regularization	Near pixels	Weights	Case	a-priori search range	Regularization	Near pixels	Weights
1	±30%	no	no	-	9	±50%	no	no	-	17	±70%	no	no	-
2	±30%	no	yes	1, 1, 1	10	±50%	no	yes	1, 1, 1	18	±70%	no	yes	1, 1, 1
3	±30%	no	yes	1.5, 1, 1.5	11	±50%	no	yes	1.5, 1, 1.5	19	±70%	no	yes	1.5, 1, 1.5
4	±30%	no	yes	2, 1, 2	12	±50%	no	yes	2, 1, 2	20	±70%	no	yes	2, 1, 2
5	±30%	yes	no	-	13	±50%	yes	no	-	21	±70%	yes	no	-
6	±30%	yes	yes	1, 1, 1	14	±50%	yes	yes	1, 1, 1	22	±70%	yes	yes	1, 1, 1
7	±30%	yes	yes	1.5, 1, 1.5	15	±50%	yes	yes	1.5, 1, 1.5	23	±70%	yes	yes	1.5, 1, 1.5
8	±30%	yes	yes	2, 1, 2	16	±50%	yes	yes	2, 1, 2	24	±70%	yes	yes	2, 1, 2

. The columns are referred to the use of Tb at 52.5° incidence angle (left), 52.5° and 57.5° (center), 47.5° 52.5° and 57.5° (right). The top row reports the RMSE and the mean bias computed between SMOS and model data for all the pixel along the transect, the center and bottom rows represent the error for *G* and *M* respectively at Dome C (light colors) and Vostok Lake (dark colors).

Figure 2-9 points out that the RMSE and mean bias tend to decrease as the number of angles considered increases. However, at the same time the algorithm estimates optimal values of the pair (*G*, *M*) worsen for the three angle case than for the two angle one (in particular for *M*). Because the improvement of the em performances is weaker than the one in the geophysical parameters, the configuration of CF with 3 angles is disregarded and the one with 52.5 and 57.7 deg chosen.

The selection of the other parameters of the CF configuration can be done by analysing the retrieval of the (G_{opt}, M_{opt}) since the variations of RMSE and bmean bias are quite negligible. By avoiding all the configurations that lead to an error on M greater than 2 cm/yr, it came out that the best configuration is the one that considers the regularization and excludes near pixels with a resulting RMSE of 0.46K and a mean bias of 0.26K. It should be noticed that this result is independent of the G search range (M one was kept fixed at a-priori $\pm 20\%$) thus, in order to be conservative it was chosen a range of a-priori $\pm 50\%$. The final configuration is reported in Table 2-4. In Figure 2-10 are reported the fitting of the SMOS measurements and the values of the cost function (also splitted in its components) as a function of the distance from Dome C.

Table 2-4: Final configuration of the Cost Function

Case	Incidence angles	G a-priori search range	Regularization	Near pixels	Weights
13	52.5°, 57.5°	$\pm 50\%$	yes	no	-

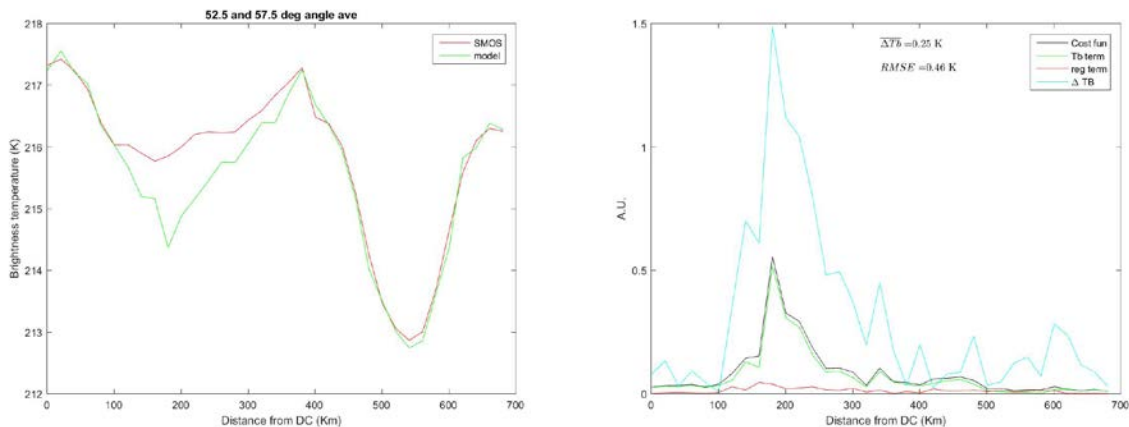


Figure 2-10: Measured (red) and fitted (green) TbV along the transect from Dome C to Vostok Lake (left), values of the Cost Function (black) and its components Tb_MSE (green) and regularization term (red) along the transect (right). Along with the Cost Function is represented also the difference between measured and fitted Tb (light blue).

2.2.5 Retrieval Products

The iterative procedure is run, it output a map of optimal pairs (G_{opt}, M_{opt}) to be used as input to the glaciological model for the calculation of the temperature profile at different depths along with the maps of surface temperature T_s and ice thickness H .

The final product of the procedure is the temperature profile of Antarctica at different depths. Areas where Robin model is not valid are masked out and a quality flag with the confidence of the estimation also provided as described in section 2.2.4.1. Secondary product are the geothermal heat flux and snow accumulation maps at the same spatial resolution of SMOS.

The quality has been classified on the basis of the score of the minimum Cost Function. Low quality (quality=2) is assigned to areas where the CF value is higher than 2, while the best quality (quality=0) is for CF lower than 1.5 as shown in Table 2-5. Moreover the retrieval of the ice sheet temperature is flagged “low quality” is performed in the regions characterized by a surface balance velocity between 5 m/yr and 10 m/yr (as described in sec 2.2.4.1).

Identification and quantification of potential error sources in the retrieval process are described in detail in D6.2 document.

Table 2-5 : Values associated to the different quality of temperature profile retrieval

FLAG VALUE	QUALITY	CONDITIONS
0	good	$CF \leq 1.5$
1	medium	$1.5 < CF \leq 2$ or $(G_{opt} = \text{a-priori} \pm 50\%)$ or $(M_{opt} = \text{a-priori} \pm 20\%)$
2	low	$(CF > 2)$ or $(5 \text{ m/yr} < \text{surf. velocity} < 10 \text{ m/yr})$
NaN	Retrieval Not Feasible	surf. velocity $\geq 10 \text{ m/yr}$

In Figure 2-11 are represented three maps of internal ice temperature estimated 250, 1000 and 2000 m deep. The maps have been masked for the Robin model validity condition, ice thickness minimum and TbV standard deviation as described in section 2.2.4.1.

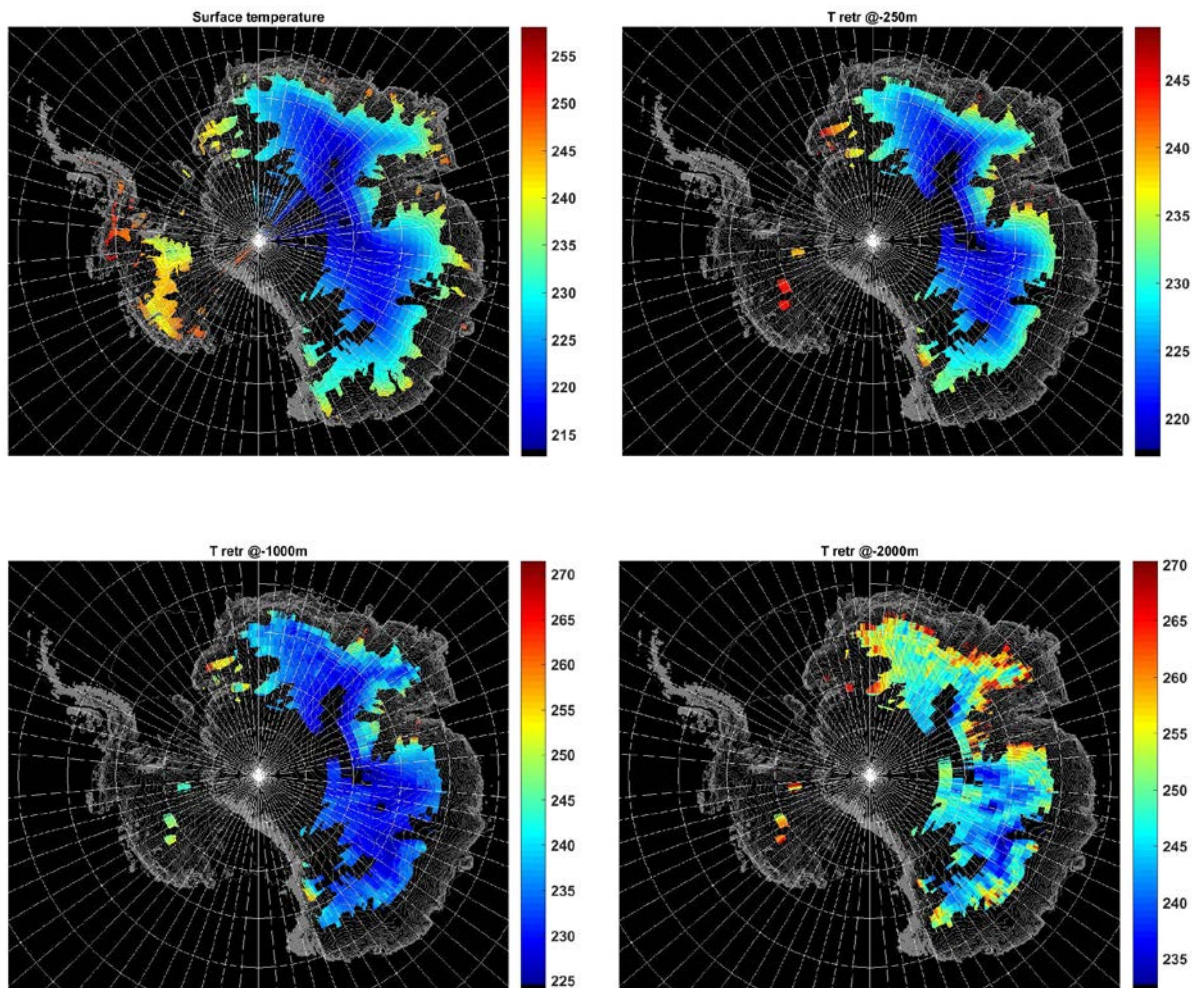


Figure 2-11: Ice sheet temperature profile retrieved. The temperature is estimated 250m below the surface (top right), 1000m deep (bottom left) and 2000m deep (bottom right). As a comparison a map of surface temperature T_s is represented (top left). The maps have been masked according to the criteria described in section 2.2.4.1.

This page is intentionally left blank

3 Case study n.2: bedrock topography and/or geothermal heat flux

(DTU in cooperation with IFAC, CESBIO)

3.1 Brief Description of the Case Study

In January 2013, the 1.4 GHz EMIRAD radiometer system was flown over a 350 km by 350 km area near the Italian/French Concordia station close to Dome-C in Antarctica (Kristensen et al., 2013; Skou et al., 2013, 2014). Vertically and horizontally polarized brightness temperature (TB) at L-band was acquired. The area is quite flat at a level of some 3000 m above sea level. A grid of 11 flight lines separated by 35 km, and a tie line crossing all other lines (for inter-comparison) was flown. The yearly mean temperature in the area is -55°C corresponding to 218 K.

The purpose of the campaign was to check the spatial homogeneity of the TB in the area. The original assumption was that the penetration depth in the ice at L-band would be such that the prime contribution to the TB would be the cold and thermally stable ice some hundreds of meters down – that is, no variations both temporal and spatial. This would constitute a well-known and stable target for calibration and inter-comparison of spaceborne L-band radiometer systems.

The measured TB, however, show unexpected variations like 8-K variation over 240 km on an east – west profile through Concordia, and in certain local cases, a slope of about 0.7 K/km. Comparing the measured TB map with bedrock topography reveals a convincing correlation. Simulations show that variations in bedrock topography, hence ice thickness, can indeed modulate the TB appropriately to explain the observed variations. It is concluded that SMOS TB maps can indicate ice thickness hence bedrock topography in Antarctica.

It is assumed that the findings over the test area near Concordia can be used over large parts of Antarctica, excluding coastal areas. Figure 3-1 shows the uncertainties in the current estimates of the ice thickness, which propagates almost directly into the uncertainty in bedrock as the surface is well known. It is evident that our interest should focus on the two large red areas (above Lake Vostok and above the South Pole in the map), where uncertainties are around 1000 m! These are not coastal areas, and especially the area near Lake Vostok will have ice properties not very different from the test area.

An important issue is the temperature profile to be used in each data point. It is the general consensus that the profiles in the interior of Antarctica must approach 270 K near the bottom due to geothermal heat. This is a very important issue in the present case. The absorption coefficient is very low at most temperatures below 270 K, but increases rapidly when approaching 270 K.

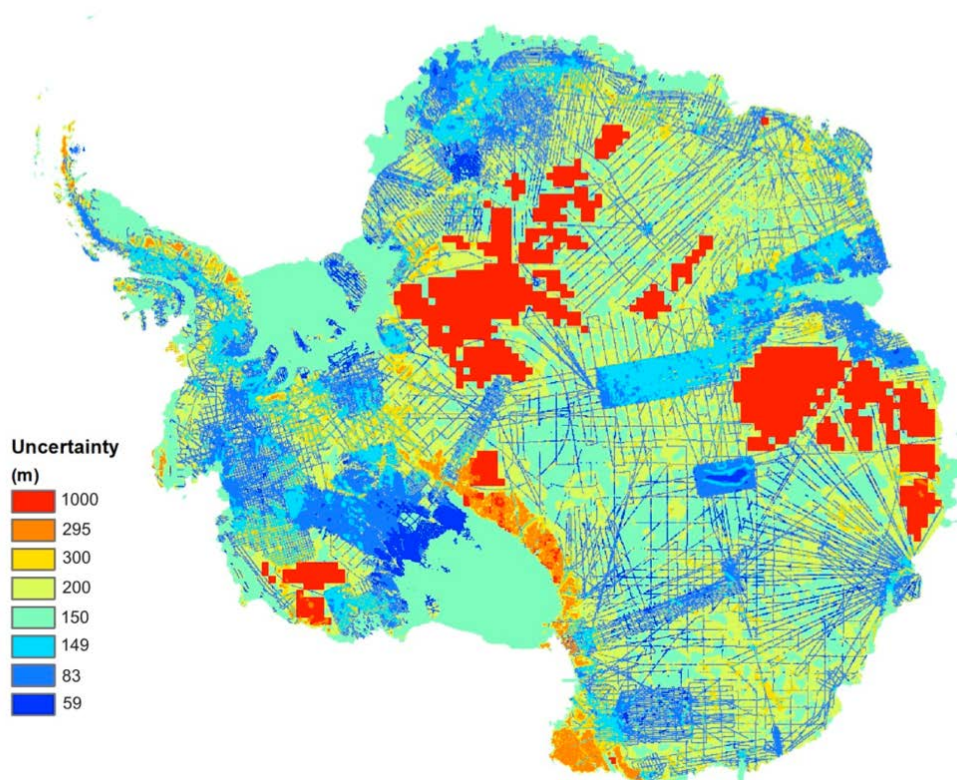


Figure 3-1: Estimated uncertainty in ice thickness

So far, simple exponential profiles have shown good results, and they have the virtue that they are forced to approach 270 K near bedrock. It has been suggested that the well known Robin model should be used [Van der Veen, 1999]. The problem with such a model is that the profile depends on a range of parameters like accumulation rate and geothermal heat flux, and it is not bound to approach 270 K near bedrock

It is noticeable that small changes in accumulation and heat flux dramatically change the temperature near bedrock where it is so important for us. Especially heat flux is not well known over the large areas of Antarctica. However, the simple exponential curves quite well represents also the Robin curves, and it was in the simulations concluded that the actual shape of the curve is not so important for the result – while it is very important that the curve approach 270 K at bedrock.

In conclusion: use a simple exponential temperature profile for each data point, forced to be 270 K near bedrock and the -10 m temperature near the ice surface.

A procedure for finding ice thickness in the large poorly known areas can now be outlined.

- Take 1 year averaged SMOS data, V pol., 45° incidence angle.
- Correct for the -10 m physical temperature
- Correlate with Bedmap in the good areas around the poorly known areas.
- Fix the relation TB to ice thickness on a rim around the unknown area.
- Through an iterative process find the ice thickness in the unknown area to fit the corrected TB map
- Find bedrock using surface elevation.
- Do the same over a well known area in order to assess retrieval accuracy

3.2 Correction for -10 m Physical Temperature.

In the campaign area around Concordia ALBMAP shows that the -10 m physical temperature varies from 228 K to 219 K, i.e. a variation of 9 K. This is why our different analyses carried out so far have used data from south of 74° S, where the temperature is quite uniform with variations below 3 K. However, in the more general cases it is necessary to take physical temperature variations into account.

First, we take the temperature profile and TB simulations already done in WP400 as a starting point. Table 3-1 is the same as shown as Table 3-3 in the D5-1 report. The surface temperature was here assumed to be 219 K.

CRYSMOS
ESA contract No.4000112262/14/I-NB

Table 3-1: Temperature, absorption, and TB for the 4000 m case,-10 m temperature is 219 K

x (m)	Exp1 temperature			Exp2 temperature			Linear temperature		
	temp (K)	100 m abs	TB (K)	temp (K)	100 m abs	TB (K)	temp (K)	100 m abs	TB (K)
0	270,0	0,723	270,8	270,0	0,724	270,8	270,0	0,724	270,8
100	265,1	0,567	267,6	267,2	0,630	268,5	268,7	0,681	269,4
200	260,7	0,450	264,5	264,5	0,550	266,3	267,5	0,639	268,2
300	256,6	0,361	261,6	261,9	0,481	264,2	266,2	0,600	267,0
400	253,0	0,294	259,1	259,4	0,421	262,2	264,9	0,562	265,8
500	249,7	0,243	256,8	257,1	0,371	260,3	263,6	0,526	264,7
600	246,7	0,205	254,7	254,9	0,327	258,5	262,4	0,492	263,5
700	244,0	0,176	252,9	252,8	0,290	256,9	261,1	0,460	262,4
800	241,6	0,155	251,1	250,8	0,258	255,3	259,8	0,430	261,3
900	239,4	0,139	249,5	248,8	0,232	253,8	258,5	0,401	260,2
1000	237,4	0,126	248,0	247,0	0,209	252,4	257,3	0,373	259,1
1100	235,5	0,117	246,5	245,3	0,189	251,0	256,0	0,348	258,0
1200	233,9	0,110	245,1	243,6	0,173	249,8	254,7	0,324	256,9
1300	232,4	0,105	243,8	242,1	0,159	248,5	253,4	0,301	255,9
1400	231,0	0,101	242,5	240,6	0,147	247,4	252,2	0,280	254,8
1500	229,8	0,098	241,2	239,1	0,137	246,2	250,9	0,260	253,8
1600	228,7	0,096	240,0	237,8	0,129	245,1	249,6	0,242	252,8
1700	227,7	0,094	238,9	236,5	0,122	244,1	248,3	0,225	251,8
1800	226,8	0,093	237,7	235,2	0,116	243,1	247,1	0,209	250,8
1900	226,0	0,092	236,7	234,1	0,111	242,1	245,8	0,194	249,8
2000	225,2	0,092	235,6	232,9	0,107	241,1	244,5	0,181	248,9
2100	224,5	0,091	234,6	231,9	0,103	240,1	243,2	0,169	247,9
2200	223,9	0,091	233,6	230,9	0,101	239,2	242,0	0,158	247,0
2300	223,4	0,091	232,7	229,9	0,098	238,3	240,7	0,148	246,0
2400	222,9	0,090	231,8	229,0	0,097	237,4	239,4	0,139	245,1
2500	222,4	0,090	231,0	228,1	0,095	236,5	238,1	0,131	244,2
2600	222,0	0,090	230,1	227,3	0,094	235,6	236,9	0,124	243,3
2700	221,6	0,090	229,4	226,5	0,093	234,8	235,6	0,117	242,4
2800	221,3	0,090	228,6	225,7	0,092	233,9	234,3	0,112	241,5
2900	221,0	0,090	228,0	225,0	0,092	233,1	233,0	0,107	240,6
3000	220,7	0,090	227,3	224,3	0,091	232,3	231,8	0,103	239,7
3100	220,4	0,090	226,7	223,6	0,091	231,5	230,5	0,100	238,8
3200	220,2	0,090	226,1	223,0	0,091	230,8	229,2	0,097	237,8
3300	220,0	0,090	225,5	222,4	0,090	230,0	227,9	0,095	236,9
3400	219,8	0,090	225,0	221,9	0,090	229,3	226,7	0,093	235,9
3500	219,6	0,090	224,5	221,3	0,090	228,6	225,4	0,092	235,0
3600	219,5	0,090	224,1	220,8	0,090	227,9	224,1	0,091	234,0
3700	219,3	0,090	223,7	220,3	0,090	227,2	222,8	0,090	233,0
3800	219,2	0,090	223,3	219,9	0,090	226,5	221,6	0,090	231,9
3900	219,1	0,090	222,9	219,4	0,090	225,9	220,3	0,090	230,9
4000	219,0	0,090	222,5	219,0	0,090	225,3	219,0	0,090	229,8

Table 3-2 shows the same simulation, but now arranged so that the surface temperature is 228K.

CRYSMOS
ESA contract No.4000112262/14/I-NB

Table 3-2: Temperature, absorption, and TB for the 4000 m case,-10 m temperature is 228 K

x (m)	Exp1 temperature			Exp2 temperature			Linear temperature		
	temp (K)	100 m abs	TB (K)	temp (K)	100 m abs	TB (K)	temp (K)	100 m abs	TB (K)
0	270,1	0,727	270,9	270,1	0,728	270,9	270,0	0,724	270,8
100	266,2	0,601	268,1	267,9	0,653	268,9	269,0	0,688	269,5
200	262,7	0,501	265,4	265,8	0,588	267,1	267,9	0,654	268,5
300	259,5	0,422	262,9	263,7	0,530	265,3	266,9	0,621	267,5
400	256,6	0,359	260,6	261,8	0,478	263,6	265,8	0,589	266,5
500	253,9	0,309	258,5	260,0	0,433	262,0	264,8	0,558	265,5
600	251,5	0,270	256,6	258,2	0,393	260,5	263,7	0,528	264,6
700	249,3	0,238	254,9	256,5	0,358	259,1	262,7	0,500	263,6
800	247,3	0,212	253,3	254,9	0,327	257,7	261,6	0,473	262,7
900	245,5	0,191	251,8	253,3	0,299	256,4	260,6	0,447	261,7
1000	243,8	0,174	250,4	251,9	0,275	255,1	259,5	0,423	260,8
1100	242,3	0,161	249,1	250,4	0,254	254,0	258,5	0,399	259,8
1200	240,9	0,150	247,9	249,1	0,235	252,8	257,4	0,377	258,9
1300	239,7	0,141	246,7	247,8	0,218	251,7	256,4	0,355	258,0
1400	238,5	0,133	245,6	246,6	0,203	250,7	255,3	0,335	257,1
1500	237,5	0,127	244,6	245,4	0,190	249,7	254,3	0,315	256,2
1600	236,6	0,122	243,6	244,2	0,179	248,7	253,2	0,297	255,3
1700	235,7	0,118	242,7	243,2	0,168	247,8	252,2	0,280	254,4
1800	234,9	0,114	241,8	242,1	0,159	246,9	251,1	0,263	253,5
1900	234,2	0,111	241,0	241,1	0,151	246,0	250,1	0,248	252,7
2000	233,6	0,109	240,1	240,2	0,144	245,2	249,0	0,234	251,8
2100	233,0	0,107	239,4	239,3	0,138	244,4	248,0	0,220	251,0
2200	232,4	0,105	238,7	238,4	0,133	243,6	246,9	0,207	250,1
2300	231,9	0,104	238,0	237,6	0,128	242,8	245,9	0,195	249,3
2400	231,5	0,102	237,3	236,8	0,123	242,1	244,8	0,184	248,5
2500	231,1	0,101	236,7	236,1	0,120	241,3	243,8	0,174	247,6
2600	230,7	0,100	236,1	235,3	0,116	240,6	242,7	0,164	246,8
2700	230,4	0,100	235,5	234,6	0,113	240,0	241,7	0,155	246,0
2800	230,1	0,099	235,0	234,0	0,111	239,3	240,6	0,147	245,2
2900	229,8	0,098	234,5	233,4	0,108	238,7	239,6	0,140	244,4
3000	229,6	0,098	234,0	232,8	0,106	238,0	238,5	0,133	243,6
3100	229,3	0,097	233,5	232,2	0,104	237,4	237,5	0,127	242,9
3200	229,1	0,097	233,1	231,6	0,103	236,8	236,4	0,121	242,1
3300	228,9	0,096	232,7	231,1	0,101	236,2	235,4	0,116	241,3
3400	228,8	0,096	232,3	230,6	0,100	235,7	234,3	0,112	240,5
3500	228,6	0,096	232,0	230,1	0,099	235,1	233,3	0,108	239,7
3600	228,5	0,096	231,6	229,7	0,098	234,6	232,2	0,104	238,9
3700	228,3	0,095	231,3	229,2	0,097	234,1	231,2	0,101	238,2
3800	228,2	0,095	231,0	228,8	0,096	233,6	230,1	0,099	237,4
3900	228,1	0,095	230,7	228,4	0,096	233,1	229,1	0,097	236,6
4000	228,0	0,095	230,5	228,0	0,095	232,6	228,0	0,095	235,7

As seen from the 2 tables, the 9 K variation in the -10 m physical temperature lead to the following changes in TB:

Profile	TF = 219 K	TF = 228 K	Δ TB
exp1	222.5	230.5	8.0
exp2	225.3	232.5	7.2
lin	229.8	235.7	5.9

For the profile exp2, which is the most realistic, we see that the 9K variation in the -10 m physical temperature lead to a 7 K variation in TB. This indicates that the TB has to be corrected for physical temperature with a factor of $7/9 = 0.78$.

Figure 3-2 shows the scatter plots for our test area around Concordia already shown as Figure 3-10 in the D5-1 report.

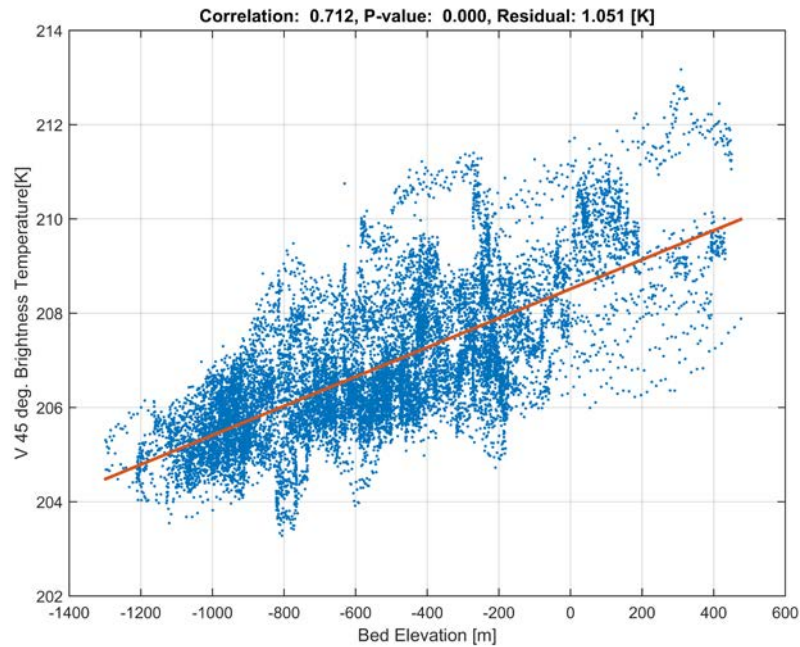


Figure 3-2: TB vs. bed elevation, south of 74°

The figure shows the good correlation of TB versus bed elevation in the area south of 74° where the physical temperature is quite constant. The rather constant temperature is also illustrated in Figure 3-3.

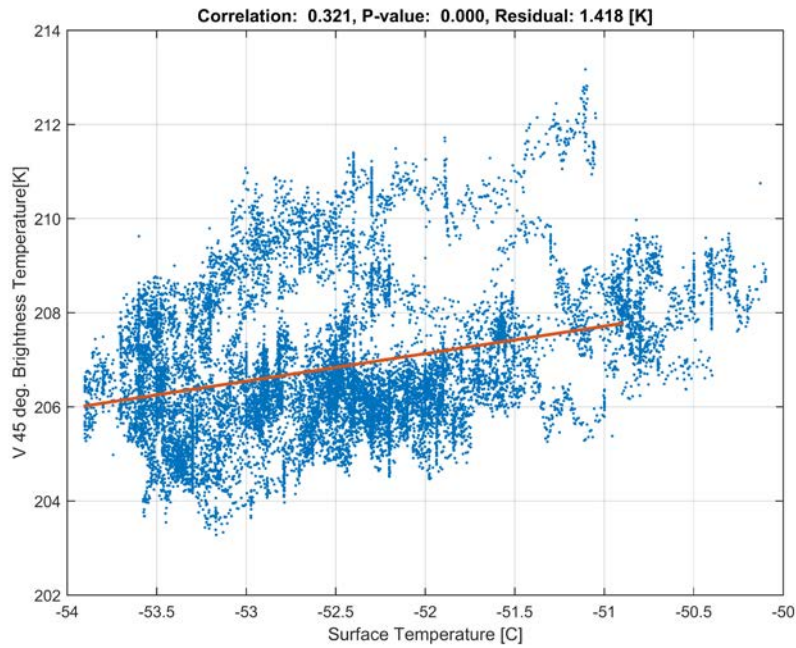


Figure 3-3: TB vs. surface temperature, south of 74°

Figure 3-4 shows the correlation TB versus bed elevation after having corrected for physical temperature. The improvement relative to Figure 3-2 is marginal, due to the modest temperature variations over the area.

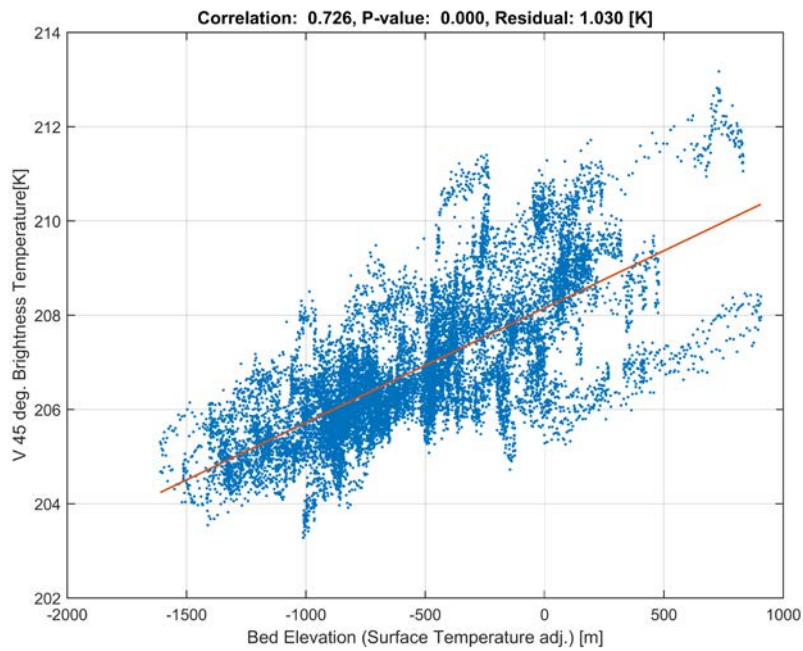


Figure 3-4: TB vs. bed elevation, temp. corr., south of 74°

Figure 3-5 shows the correlation TB versus bed elevation for the total test area. Surely the scatter is larger than in Figure 3-2 as expected now the temperature is not nearly constant.

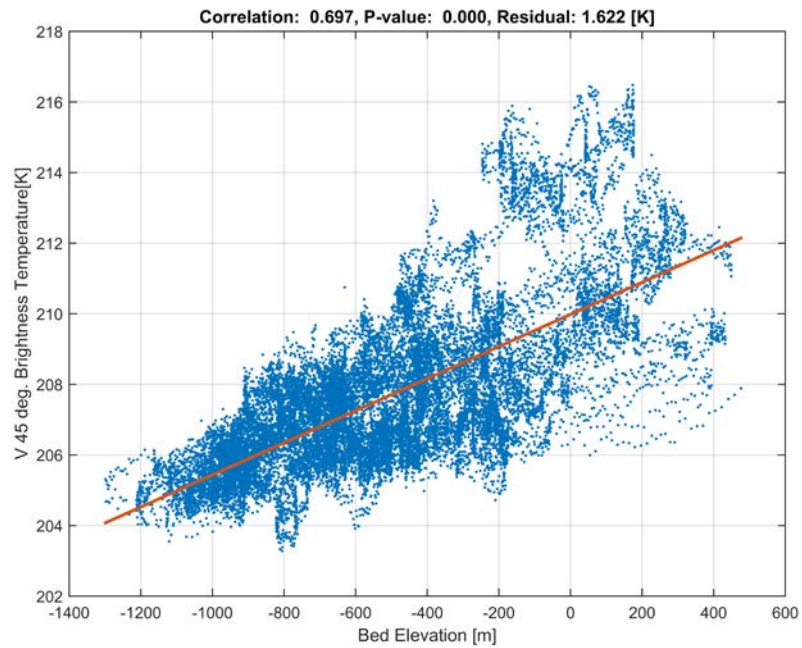


Figure 3-5: TB vs. bed elevation, full area

Figure 3-6 shows the scatter of TB versus temperature, and the variations are of course much larger than in Figure 3-2.

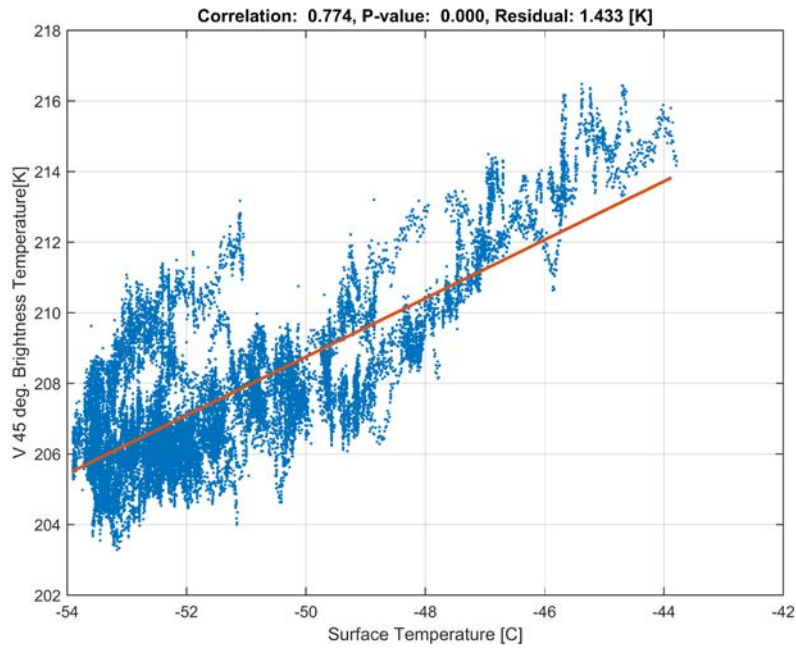


Figure 3-6: TB vs. surface temperature, full area

Figure 3-7 shows the scatter plot TB versus bed elevation for the full area, but now compensated for temperature variations. The result is quite good with a large correlation coefficient and modest scatter around the regression line.

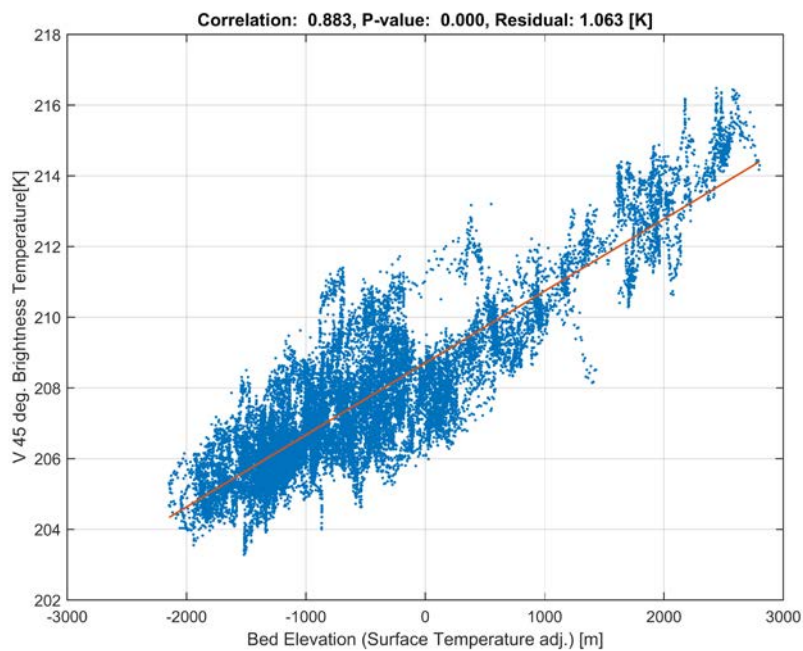


Figure 3-7: TB vs. bed elevation, temp. corr., full area

Returning to Figure 3-6 we see that TB has to be corrected for physical temperature with a factor of 0.77. This corresponds very well with the factor 0.78 found from the temperature profile simulations.

Conclusion: TB has to be corrected for variations in the -10 m physical temperature. Presently a correction factor of 0.77 seems valid.

3.3 DomeC ice thickness estimation

In order to verify the bedrock estimation from brightness temperature a linear regression was performed using EMIRAD data from the 2013 Antarctica campaign area near Concordia. Figure 3-8 shows the correlation between brightness temperature and ice thickness.

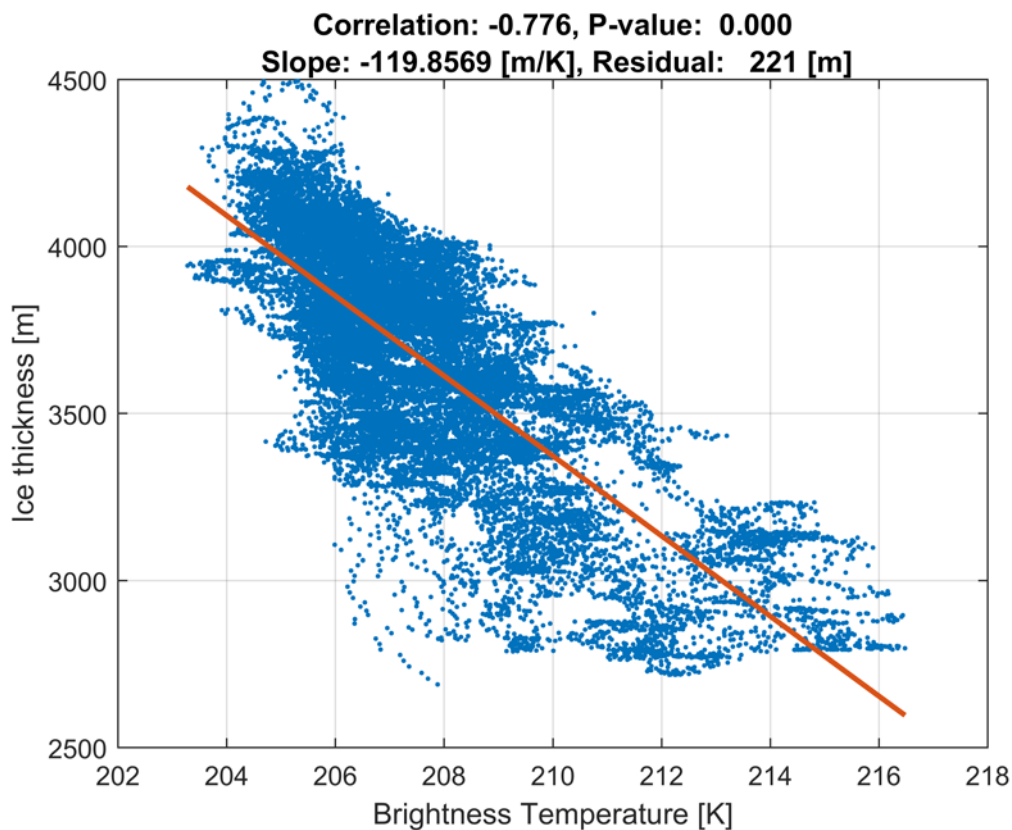


Figure 3-8: The ice thickness estimated from brightness temperature.

The model used in Figure 3-8 is

$$(\text{Ice Thickness}) = \beta_1 + \beta_2 * (\text{Brightness Temperature}) \quad (3.1)$$

To incorporate the -10 m temperature dependence the above model was expanded to:

$$(\text{Ice Thickness}) = \beta_1 + \beta_2 * (\text{Brightness Temperature}) + \beta_3 * (-10 \text{ m Temperature}) \quad (3.2)$$

The regression parameters are:

Model	β_1 [m]	β_2 [m/K]	β_3 [m/K]
Brightness Temp.	28543.86	-119.86	NA
Brightness Temp. adj	40004.71	-160.98	56.92

By rewriting the model to

$$(\text{Ice Thickness}) = \beta_1 + \beta_2 * [(\text{Brightness Temperature}) + \beta_3/\beta_2 * (-10 \text{ m Temperature})] \quad (3.3)$$

And the unit in the square bracket can be regarded as the surface temperature adjusted brightness temperature. The result is shown in Figure 3-9.

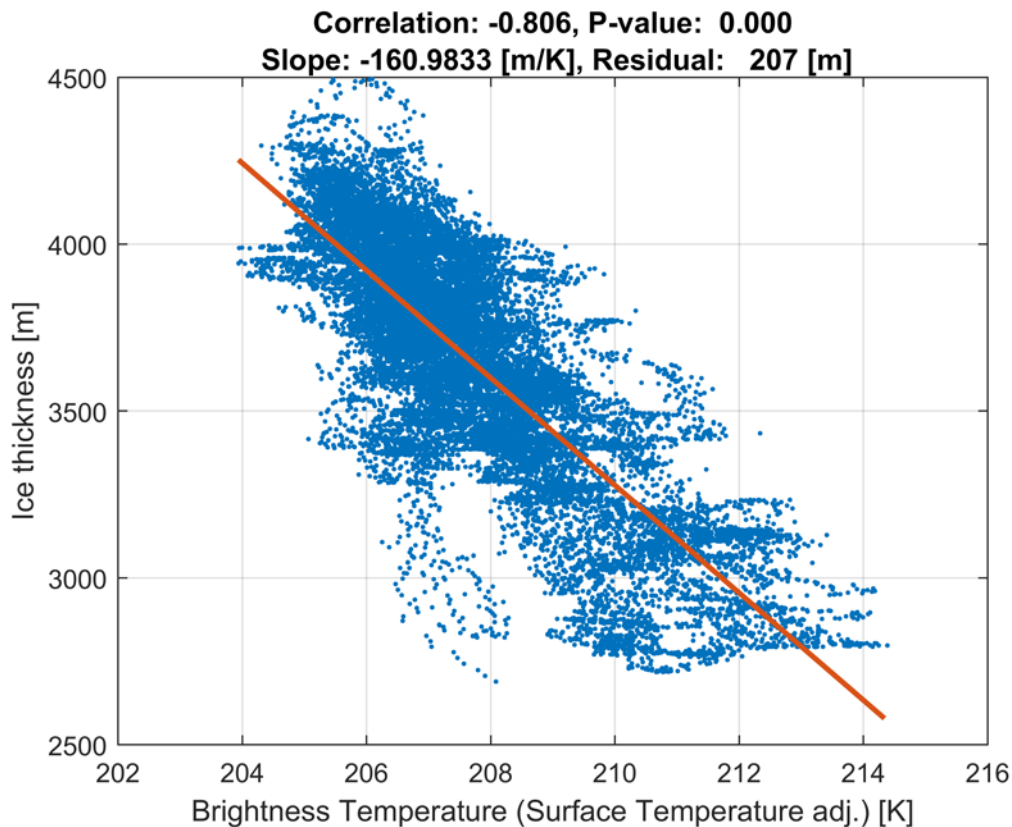


Figure 3-9: The ice thickness estimated from surface temperature adjusted brightness temperature.

It can be seen that the residual error (standard deviation of the difference between the ice thickness data and estimate) on the ice thickness is approximately 200 m, which is in accordance with the uncertainties of the area near Concordia as shown in Figure 3.1. With other areas having uncertainties up to a 1000 m it is obvious to try to estimate ice thickness and thereby bedrock from SMOS data in such areas.

3.4 East Antarctica ice thickness estimation from SMOS data

The method described above is not directly applicable for SMOS data. Due to the much larger SMOS sample footprint the method described above becomes numerically unstable, wherefore, another approach must be applied.

The brightness temperature radiated from a body, T_b , with a physical temperature, T_{phys} , is given by

$$T_b = e * T_{phys}, \quad (3.4)$$

where e is the emissivity. The physical temperature increases from the surface temperature to approximately 270 °C at bedrock as modelled above and the brightness temperature is a combination

of the surface radiation and the radiation below the surface. The contribution from below the surface should increase as the ice thickness decreases assuming that the penetration at L-band is independent of the temperature profile. Thus a simple and numerically stable method would be:

$$(\text{Ice Thickness}) = \beta_1 + \beta_2 * (T_b - e * T_{\text{phys}}) \quad (3.5)$$

To verify this method the same area around Concordia where EMIRAD data was used as described above has been selected. The SMOS brightness temperature of this area is shown in Figure 3-10. The elongated samples shown in Figure 3-10 reflect the sampling of SMOS scientific data in the Polar Regions used in this project.

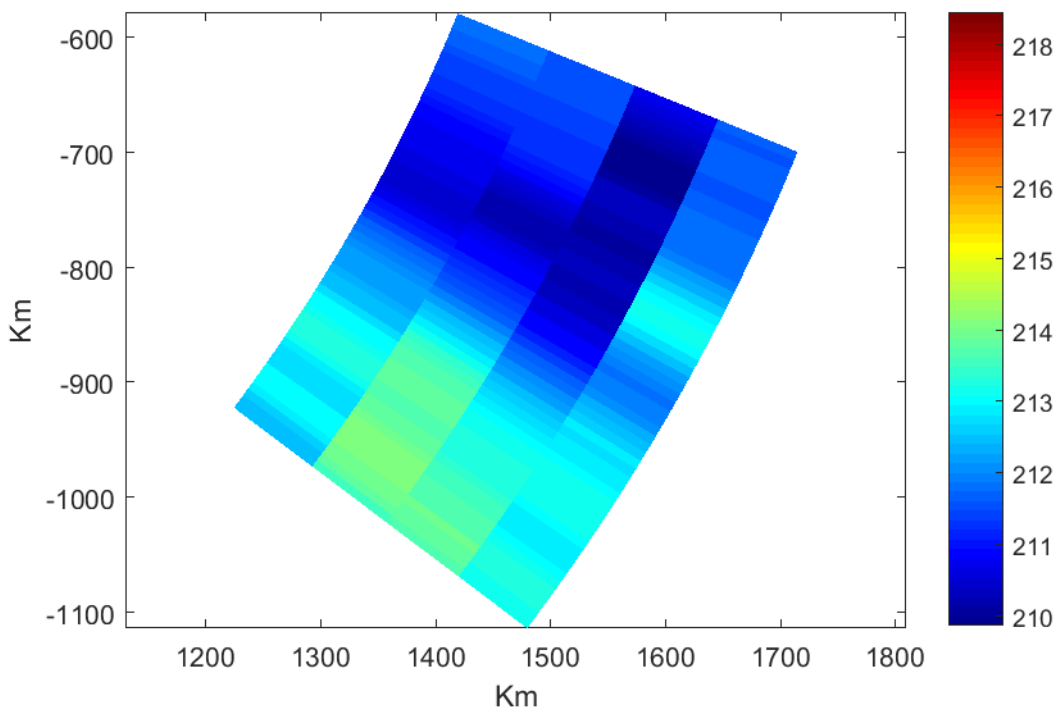


Figure 3-10: SMOS brightness temperature in the Concordia area.

Varying the emissivity from zero to one and calculating the correlation between ice thickness and $T_b - e * T_{\text{phys}}$ provides the curve shown in Figure 3-11.

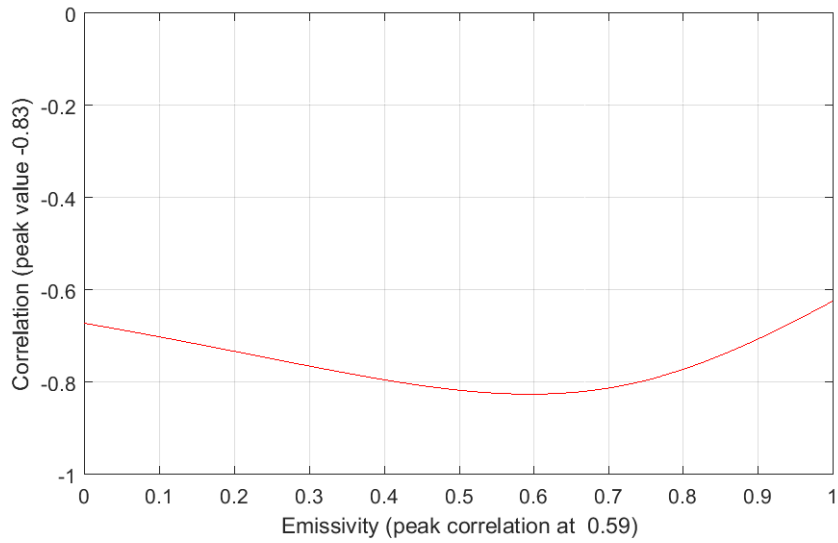


Figure 3-11: Concordia area; correlation between ice thickness and $T_b - e * T_{phys}$.

It is seen that a peak correlation of -0.83 is achieved for an emissivity of 0.59. This correlation is in accordance with the values obtained using EMIRAD data. The low value of the emissivity probably reflects the simple models. Applying the model above and using the ice thickness shown in Figure 3-12 provides the results shown in Figure 3-13.

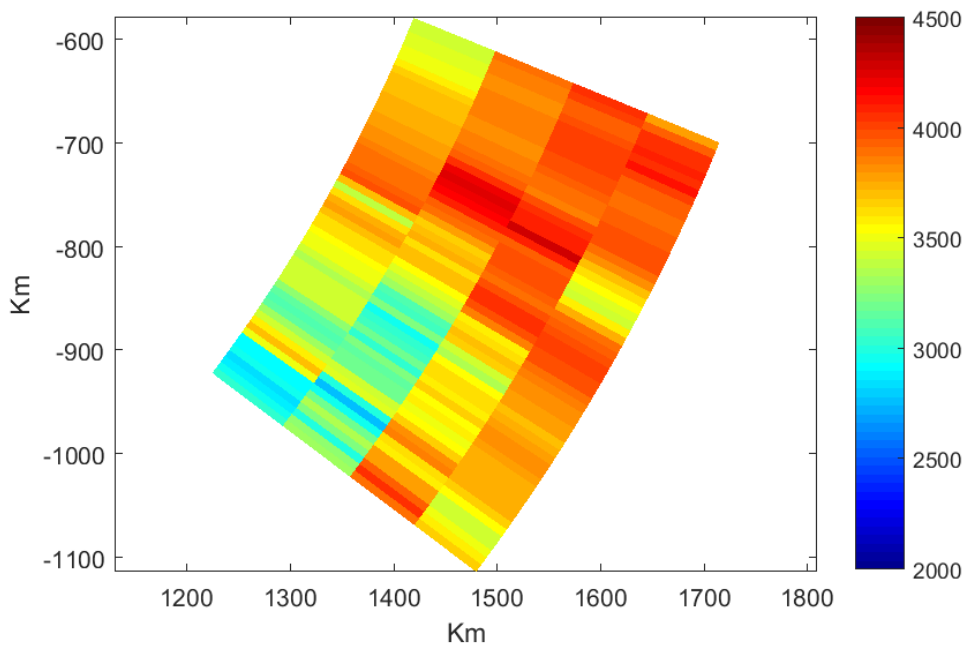


Figure 3-12: Bedmap ice thickness around Concordia.

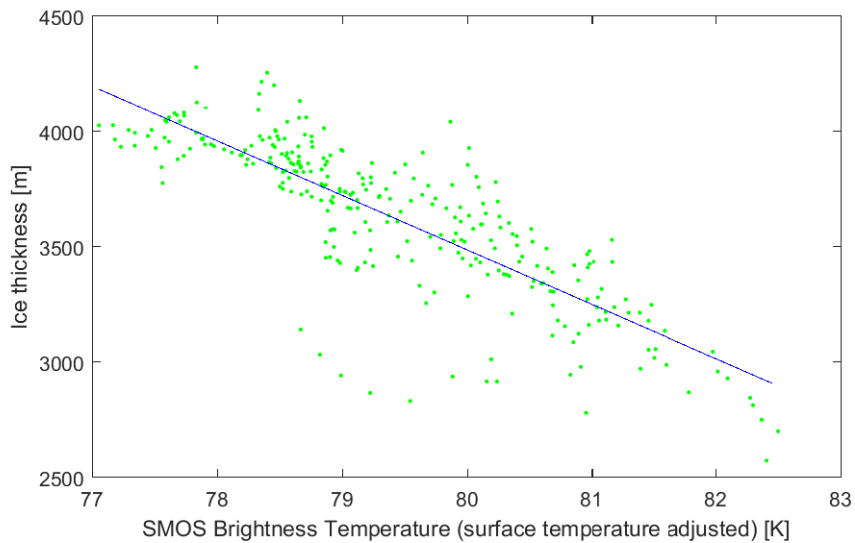


Figure 3-13: Concordia area; scatter plot of ice thickness vs. surface temperature adjusted SMOS brightness temperature and regression line.

The residual error using this regression is 191 m is in line with the results obtained using EMIRAD data as expected and in the same order as the bedmap uncertainty in the area. The model thus seems valid when substituting EMIRAD data with SMOS data and it is therefore appropriate to use a larger area for verification such as an angular section of Antarctica covering the Concordia area as shown in Figure 3-14 and 3-15. Hereafter denoted extended Concordia area.

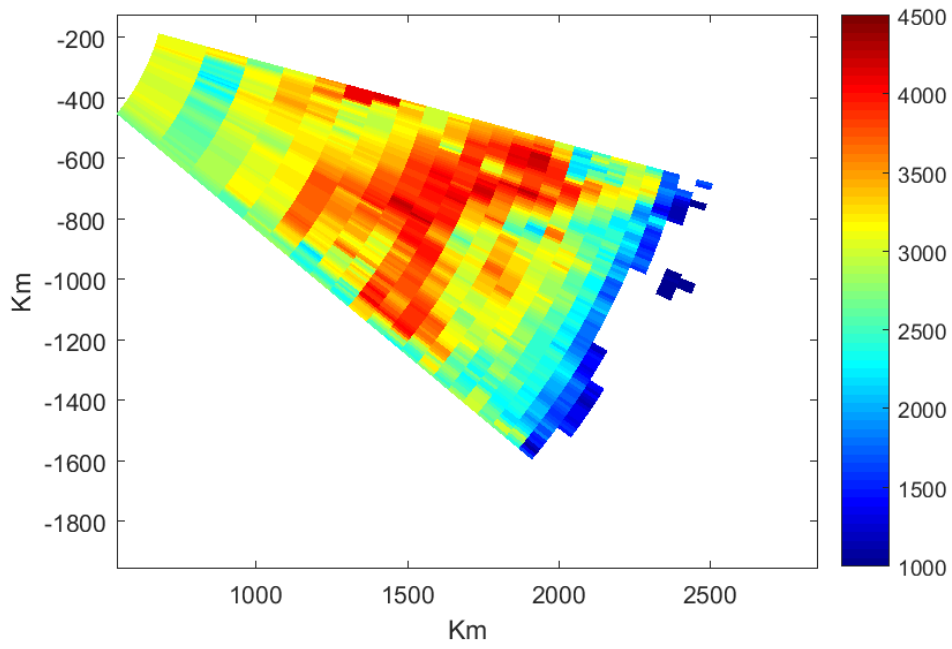


Figure 3-14: Extended Concordia area Bedmap ice thickness.

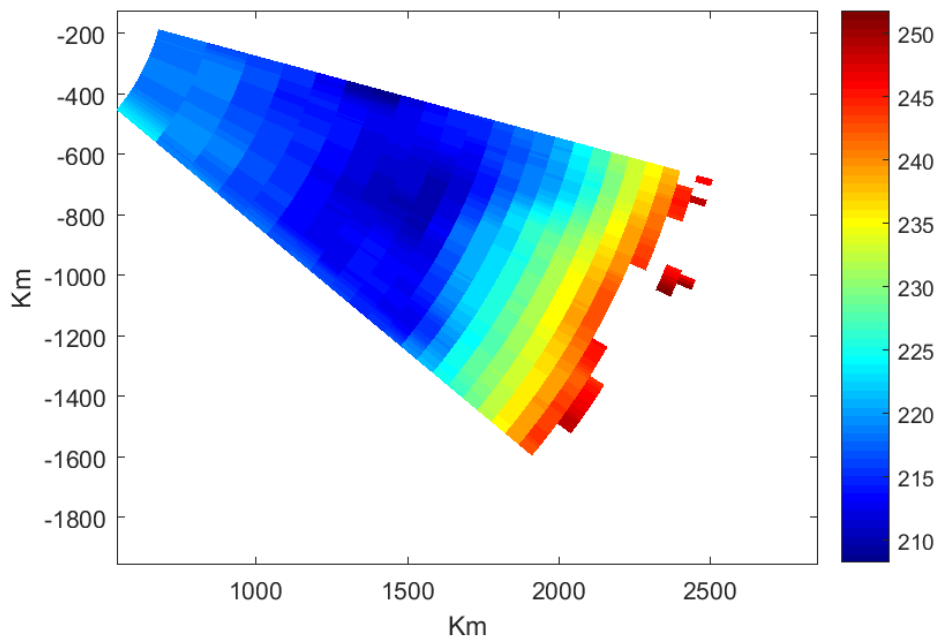


Figure 3-15: Extended Concordia area SMOS brightness temperature.

To avoid effects due to surface melting and freezing all samples with a surface altitude below 1000 m have been excluded from the extended Concordia area shown in Figures 3-14 and 3-15. For this area the emissivity dependent correlation is provided in Figure 3-16.

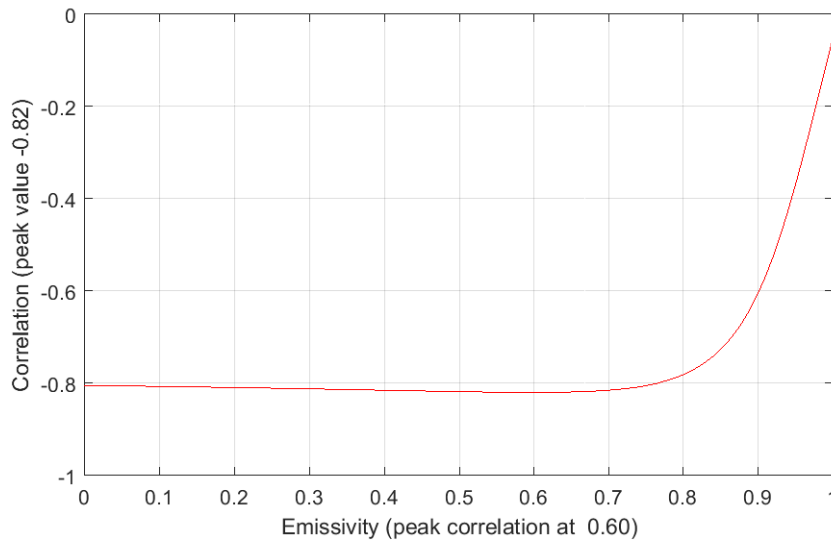


Figure 3-16: Extended Concordia area; correlation between ice thickness and $T_b - e * T_{phys}$.

Applying an emissivity of 0.6 provides the linear regression shown in Figure 3-17.

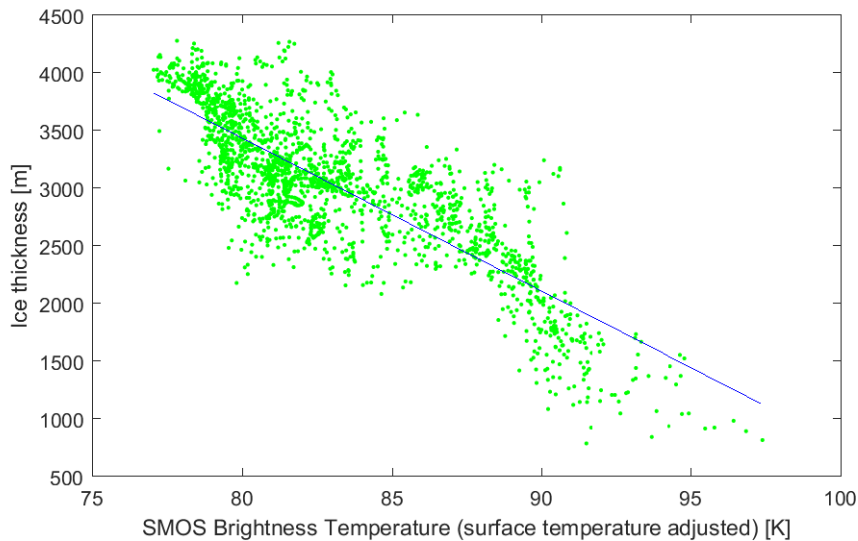


Figure 3-17: Extended Concordia area; scatter plot of ice thickness vs. surface temperature adjusted brightness temperature and regression line.

The correlation for the regression shown in Figure 3.17 is -0.82 which is well in line with the previous obtained results while the residual error has increased to 363 m. As the bedmap uncertainty is approximately the same for this area as for the area just around Concordia the increase in the residual error of the ice thickness estimate must be due to the model. It is therefore not feasible to use the model to improve the bedmap ice thickness accuracy except in areas where this uncertainty is larger, say 1000 m, the red areas in Figure 3-1. As the red areas in top of Figure 3-1 are presently being replaced by more accurate measurements and therefore no longer interesting in this context it only seems feasible to apply this model on the large red area in the right of Figure 3-1 which is next to the extended Concordia area where the model has been verified. An angular section of Antarctica including this area has been selected as shown in Figure 3-18. This area is lower limited in longitude by exclusion of the Prince Charles Mountains and upper limited in longitude by including the extended Antarctica area. To avoid effects due to surface melting and freezing all samples with a surface altitude below 1000 m have been excluded as in the extended Concordia area. The area shown in Figure 3.18 is hereafter denoted East Antarctica area.

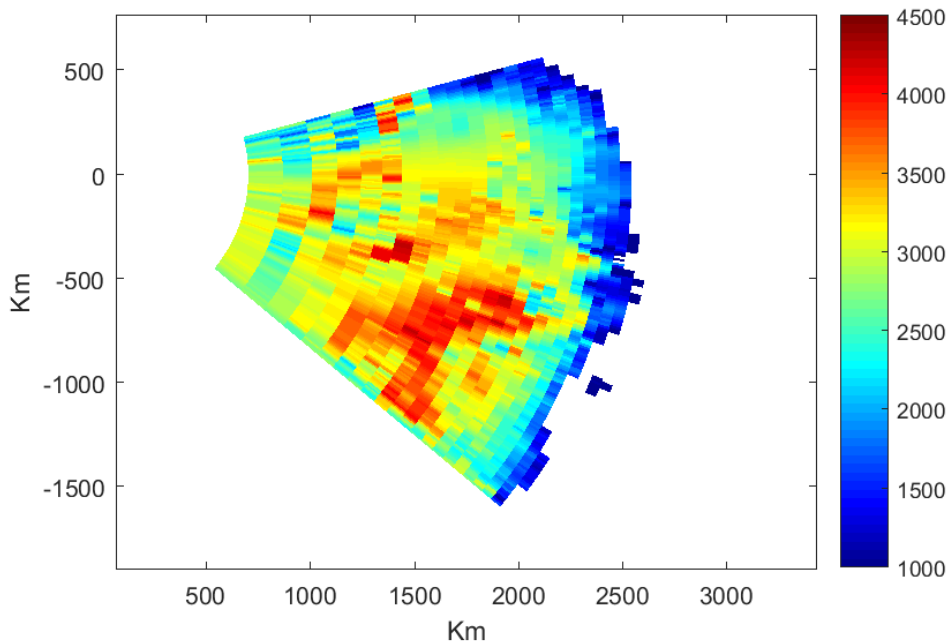


Figure 3-18: East Antarctica area Bedmap ice thickness.

The ice thickness is highly varying within the East Antarctica area except in the areas with 1000 m bedrock uncertainty marked with red in Figure 3-1. Removing samples with 1000 m uncertainty gives the data shown in Figure 3-19.

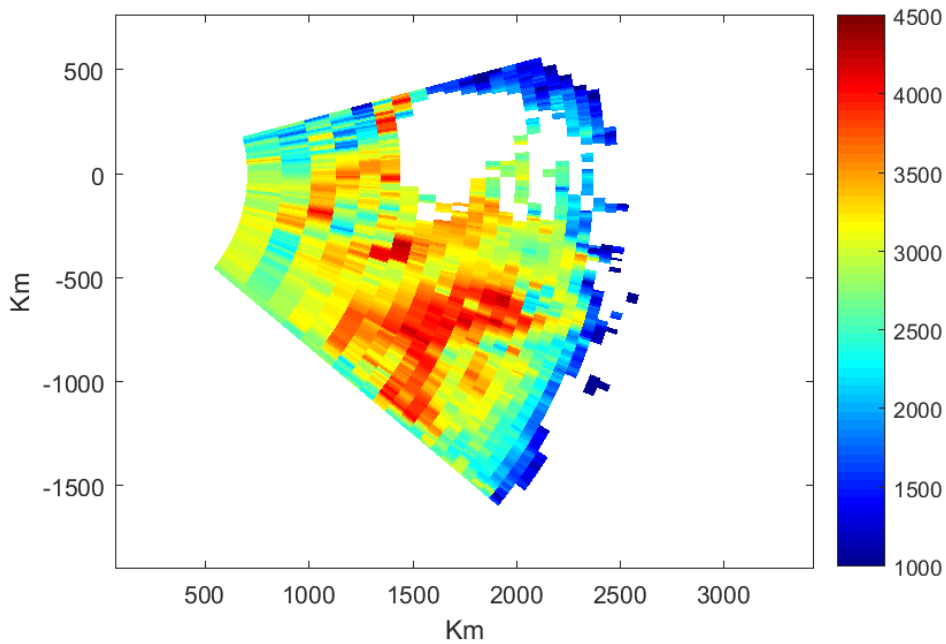


Figure 3-19: East Antarctica area Bedmap ice thickness. Samples with ice thickness uncertainty of 1000 m have been removed.

Performing the same correlation and regression as described above using the samples shown in Figure 3-19 provides the results shown in Figure 3-20 and 3-21.

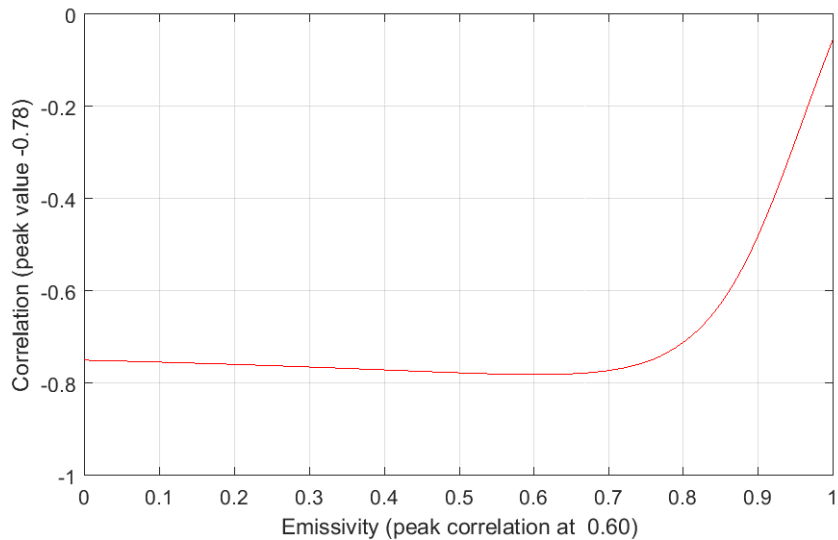


Figure 3-20: East Antarctica; correlation between ice thickness and $T_b - e * T_{phys}$.

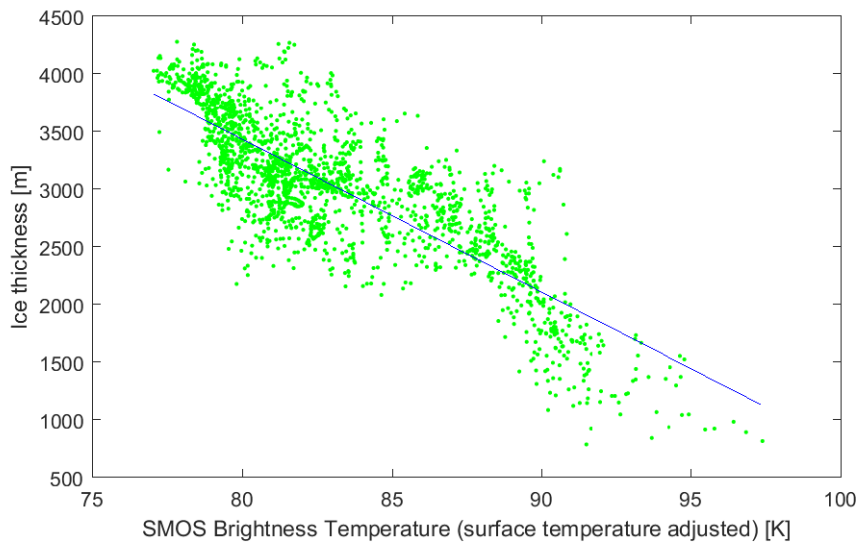


Figure 3-21: East Antarctica area; scatter plot of ice thickness vs. surface temperature adjusted brightness temperature and regression line.

The residual error has increased marginally to 420 m, so the model seems feasible. Using the regression line of Figure 3-21 to estimate the ice thickness in the area where the uncertainty is 1000 m provides the estimate shown in Figure 3-22.

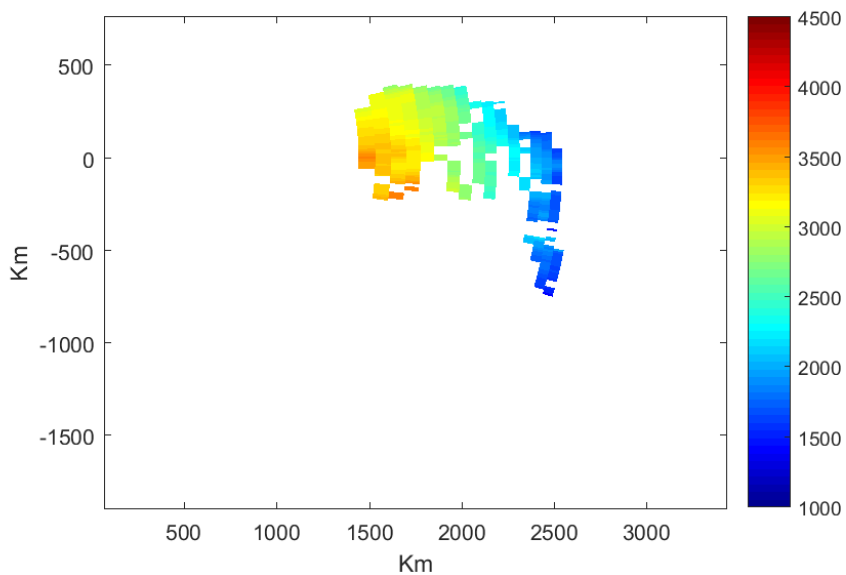


Figure 3-22: Ice thickness estimate in the area with ice thickness uncertainty of 1000 m.

Merging the estimate in Figure 3-22 with the ice thickness in Figure 3-19 gives the final result shown in Figure 3-23.

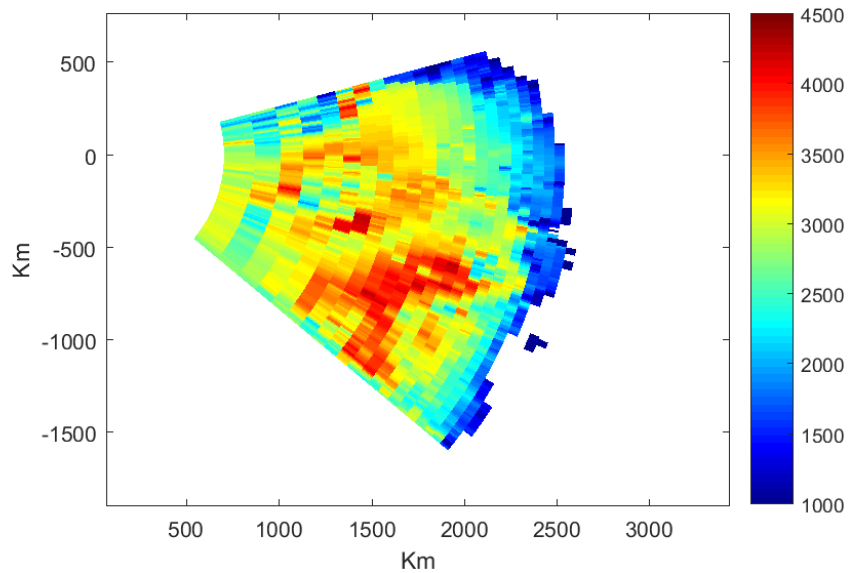


Figure 3-23: Bedmap ice thickness data patched with SMOS brightness temperature based ice thickness estimates where the bedmap uncertainty is 1000 m.

It has been shown how bedmap ice thickness in areas of high bedmap uncertainty can be replaced by ice thickness estimated based on SMOS data and surface temperature. Validation and assessment of the errors are provided in [D6-2].

This page is intentionally left blank

4 Case study n.3: characterization of ice shelves

(UHAM in cooperation with CESBIO)

4.1 Brief description of the case study

The microwave emissions in L-band from ice shelves are determined mainly by three quantities: The distance through the shelf which is covered by the electromagnetic (EM) wave, the transparency and strength of emission of the ice (determined by the loss factor/imaginary part of relative permittivity and physical temperature) as well as the surface/firn emissivity i.e. the fraction of upward emissions in the ice which enter the atmosphere (determined by the differences in relative permittivity at interfaces including the snow-air interface but also ice lenses inside the firn). The distance covered in the ice is in good approximation a linear function of the ice shelf thickness while the relative permittivity is mainly dependent on the ice temperature, density and the formation process of the ice determining the brine fraction. Physical parameters with a potential influence on the SMOS measurements, which are at the same time candidates for a retrieval, are: ice temperature and density profiles, strength of density fluctuations in the firn, the presence of marine ice and open rifts.

Ice shelf specific processes influencing the physical temperature are special ice flow profiles (due to negligible bottom strains) and average bottom heat fluxes, which can easily exceed the geothermal heat flux by a factor of 100. Marine ice freezing to the base of the shelf in some regions has not only an effect on the mechanical stability but has also very distinctive electromagnetic properties. The firn layer of ice shelves is governed by typically high accumulation rates and relative high air temperatures, which can lead to surface melt.

4.2 Characterization of the ice shelves: Retrieval Approach or Methodology – Final ATBD

4.2.1 *The Emission Model*

An incoherent multi layer ice and snow emission model with planar interfaces has been developed based on Maaß et al. (2013, and references therein). The implementation allows the use with around one thousand layers at reasonable computational costs, which enables us to set the layer thickness to 2.5 cm near the surface while still accounting for all interface reflections. The model has been adopted to ice shelves by implementing a base layer of sea water at $-2.5\text{ }^{\circ}\text{C}$ (the approximate pressure melting point) and if desired an intermediate layer of marine ice between the water and meteorological (i.e. fresh water) ice at the same temperature. Electromagnetic properties of meteorological ice and the influence of snow densities below 917 kg/m^3 are taken into account based on the empirical relations from Mätzler (2006) and Tiuri et al. (1984), respectively.

Marine ice is assumed to have similar EM properties as Baltic sea ice (Kaleschke et al., 2010) as the salinity concentrations are comparable. The typical marine ice thickness is (if present) about tens to hundreds of meters. As marine ice is opaque (non-transparent) for thicknesses above one to two meters we use a concentration c_{MI} instead of a plain layer thickness for the representation of marine ice. This means that simulations with $c_{MI} > 0$ are done with and without a thick (3 m) marine ice layer and the results are combined linearly based on c_{MI} .

Rifts penetrating the whole ice shelf are filled with a melange of broken parts of the ice shelf and sea ice. The very simple implementation of rifts in the model is a linear mixing of the emissions from the shelf and sea ice c_{RI} (one layer of 4 m multi year sea ice with 40 cm of snow at air temperature while the bulk ice temperature is neglecting the thermal insulation of the snow).

Perturbations from the mean densities ρ are simulated as zero mean Gaussian distributed random noise with standard derivation σ ($\rho_{total} = \rho + GAUSS(0, \sigma)$). The total emission is derived as the mean of multiple simulation with different noise realizations.

A relation between ρ and σ as shown in Hörhold et al. (2011) is used to couple those two parameters. A fifth order polynomial (see Table 4.1) is used to approximate σ as functions of ρ like found by borehole measurements in Queen Maud Land (line E in Hörhold et al. (2011) Fig. 7f). By doing so a local maximum of the density perturbations at roughly 30 m depth is achieved, which is often found in nature and is a substantial difference to e.g. exponential decaying profiles of σ . As there are regional differences of the density perturbation strength and as the effect on the emission is further dependent on the used layer thickness we introduce an amplification factor a_σ to account for the resulting uncertainties. The density perturbation strength σ used in the model can therefore be described as $\sigma = a_\sigma \cdot \sigma_{QML}$ where σ_{QML} is derived from the mean density based on the mentioned fit (Table 4.1). So both, σ and σ_{QML} are functions of mean density ρ and by that of the depth, while a_σ not.

A simple atmospheric correction for L-band from Peng et al. (2013) is implemented driven by a global climatology from NCEP reanalysis-1 data from the period 1948 to 2014.

Different types of functions are used for the remaining profile (i.e. depth dependent) variables to reduce the degrees of freedom (see Table 4.1). Three different temperature functions are used ranging from representing thermodynamic equilibrium (linear) to strong basal melt with corresponding downward advection (Luckman et al., 2012; Cuffey and Paterson, 2010). The parameters for the temperature are therefore reduced to surface temperature (T_s) and the chosen function (bottom temperature $T_b = -2.5^\circ C$). For the mean density we assume an exponential function reducing its free variables to the surface density (ρ) and a parameter ζ related to the thickness of densities below the density of pure ice ($\rho=917 \text{ kg/m}^3$) called firn thickness in the following.

The remaining input parameters of the model are the surface temperature (T_s), the temperature profile function (one of three), the mean surface density (ρ_s), the firm thickness (ζ), the stratification factor (a_σ), the meteorological ice thicknesses (H) and the area concentrations of marine ice (c_{MI}) and rifts (c_{RI}).

4.2.2 SMOS data

The used SMOS dataset is processed at the University of Hamburg based on the SMOS L1C version 620 data (Mecklenburg et al., 2016). The SMOS measurements are gridded daily on the Icosahedral Snyder Equal Area (ISEA) 4H9 grid. We use a fitting function from Zhao et al. (2015) to refine the characteristics of the multi-angular SMOS observations (see Fig. 4.1). It is based on a two-step regression approach.

In the first step the brightness temperature at nadir, which is the same for H and V polarizations, is estimated from the brightness temperature intensity. We approximate the nadir brightness temperature as the average of all SMOS measurements with incidence angles below 40° (also called SMOS Intensity in the following) because of the largely symmetric behaviour of the two different polarizations up to this angle. The h-polarization is slightly lower than the v-polarization but they can

be assumed to be centered at the nadir brightness temperature (Fig. 4.1). The second step relies on the nadir brightness temperature (TB_{nn}) to perform a least square fitting procedure with:

$$TB_{v,h}(TB_{nn}, \theta) = a_{v,h} \cdot \theta^2 + TB_{nn} \cdot \left(b_{v,h} \sin^2(d_{v,h} \cdot \theta) + \cos^2(d_{v,h} \cdot \theta) \right) \quad (4.1)$$

where $d_h = 1$.

We found that the fit does not yield reasonable results when the sample size of the measurements is too small. Therefore we limit the fitting procedure to cases where there are more than 15 SMOS measurements per grid point spanning an incidence angle range of more than 20° . This minimum amount of measurements is available in most regions south of 60° S.

A comparison of SMOS intensities with the distribution of marine ice beneath the Ronne-Filchner ice shelf from Lambrecht et al. (2007) gives indications for an increase in the SMOS intensity from marine ice (Fig. 4.2). This gives us some confidence that there is a contribution from deep layers of the ice shelf in the observations.

Table 4.1: Summary of used models/approximations

Property/Process	Method/Reference
Relative Permittivity Ice	Mätzler (2006)
Density dependence of Relative Permittivity	Tiuri et al. (1984)
Relative Permittivity Water	Klein and Swift (1977)
Relative Permittivity Marine Ice	Kaleschke et al. (2010)
Temperature Profiles	$T(z) = T_s + (T_b - T_s) \cdot z/H$ (linear, #1) $T(z) = T_b + (T_s - T_b) \cdot \left(\frac{H-z}{H}\right)^{\frac{1}{3}}$ (Luckman et al. (2012), #2) $T(z) = T_b + (T_s - T_b) \cdot \left(\frac{H-z}{H}\right)^{\frac{1}{5}}$ (#3)
Mean Density Profile	$\rho(z) = 917 - (917 - \rho_s) \cdot \exp\left(\frac{-z}{\zeta}\right)$ (in kg/m ³ , Bereiter et al., 2014)
Density Stratification in Firn	Method following West et al. (1996), fit to line E in Fig.7f of Hörhold et al. (2011): $\sigma_{QML} = 4.588 \cdot 10^{-12} \cdot \rho^5 - 1.612 \cdot 10^{-8} \cdot \rho^4 + 2.087 \cdot 10^{-5} \cdot \rho^3 - 1.222 \cdot 10^{-2} \cdot \rho^2 + 3.054 \cdot \rho - 201.3$ (in kg/m ³) $\sigma = a_\sigma \cdot \sigma_{QML} \rho_{total} = \rho + GAUSS(0, \sigma)$

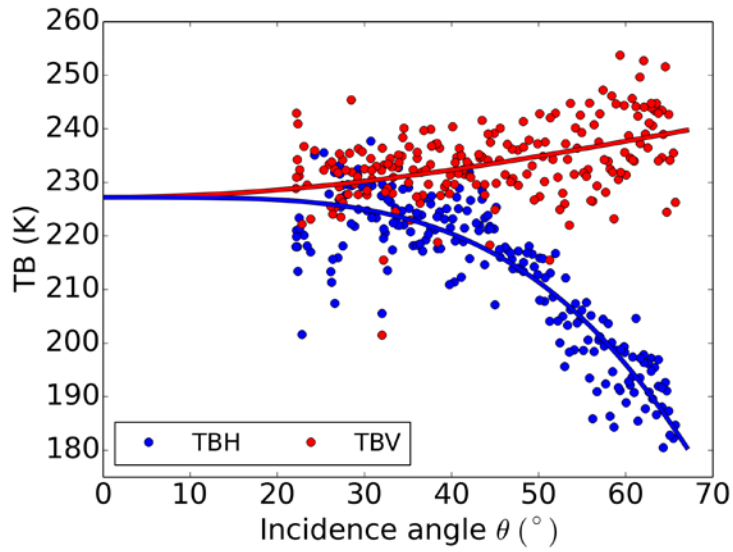


Figure 4.1: Example SMOS observations from July 05 2015 at (73.0° S, 59.58° W) on the Ronne ice shelf with used fit.

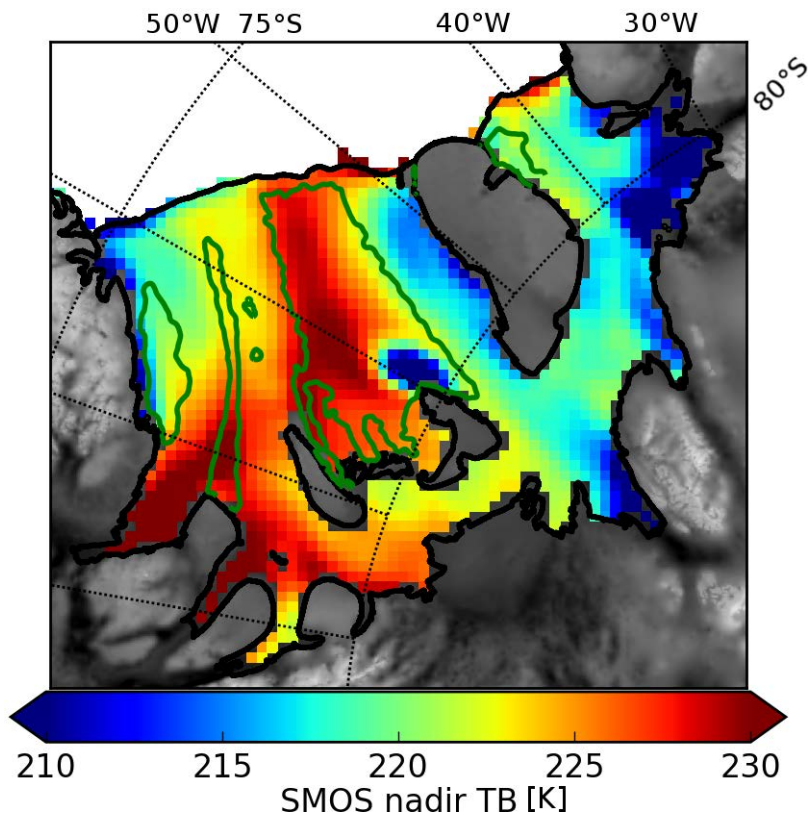


Figure 4.2: SMOS nadir TB from 2010 to 2015 at the Ronne-Filchner Ice Shelf region with contour of significant amounts of marine ice (Lambrecht et al., 2007). In addition the grounding and coast lines (black) from the MODIS Mosaic of Antarctica project 2009 and the land topography from Bedmap-2 (shades).

4.2.3 Method

As the number of model input parameters exceeds the independent information in the measurements we are facing an ill-posed retrieval problem. In addition, certain realistic combinations of input parameters show equal simulated emissions, illustrating the challenges in retrieving individual parameters. To overcome this infeasibility we separate the input parameters into two sets, namely surface + firn properties (ζ, a_σ, ρ_s , hereafter called surface properties) and internal + bottom properties ($T(z), H, c_{MI}, c_{RI}$, hereafter called bottom properties). The focus here will be on temporal variations in the SMOS measurements instead of the mean state for the following reasons. There is a high scientific interest in monitoring changes of ice shelf properties from satellites while in-situ and airborne campaigns are in most aspects more suited to draw a static picture of the ice shelf. The repetition of flights is, if done at all, very sparse in time and space. We have further stronger confidence in the model for investigating the impact of changes in parameters than we have in the absolute values (potential biases e.g. caused by uncertainties in the model of ice permittivity).

The aim is to retrieve which of this two sets is responsible of variations in the SMOS signal on a pixel by pixel basis. Two Monte Carlo setups have been used which are described in Table 4.2.

Table 4.2: Parameter distributions used for Monte-Carlo simulations

	Bottom		Surface	
	Range	Distribution	Range	Distribution
$T(z)$	#1, #2 and #3	Equal	#2	-
H	150 to 310 m	GAUSS(230, 50)	230	-
c_{MI}	0 to 1	Equal	0.20	-
c_{RI}	0 to 0.10	Equal	0	-
ζ	32 m	-	1 to 63 m	GAUSS(32, 10)
a_σ	1	-	0.5 to 1.5	GAUSS(1, 0.2)
ρ_s	450 kg/m ³	-	250 to 650 kg/m ³	GAUSS(450, 80)

Figure 4.3 shows that the relation between modeled nadir TB and normalized polarization difference at 40° (hereafter called polarization, $Pol = \frac{TB^{v40} - TB^{h40}}{0.5(TB^{v40} + TB^{h40})}$) is different for variations in bottom properties (green) and near surface properties (blue). This difference is based on the fact that emissions within a medium are non-polarized until they are transmitted across an interface (Ulaby et al., 2014).. Surface properties of ice shelves have an influence on the signal due to an intensification or reduction of interface reflections while bottom properties change mainly the amount of emissions. Some bottom

properties do modulate interfaces (like the presence of marine ice causes a marine ice - meteorological ice interface). However, the main influence of bottom properties on the signal are the changes in non-polarized emissions within the ice (TB_{ice}) which have no influence on the polarization but on the amplitude (substitute $TB^{v,h} = \epsilon^{v,h} \cdot TB_{ice}$ for Pol where $\epsilon^{v,h}$ is the emissivity for v or h polarization (Eq. 6.95 in Ulaby et al. 2014). The different signatures are exploited in the following to identify the origin of observed variations.

We take repeatedly six random model results from the same class and perform an orthogonal regression on them. From the resulting distributions of nadir TB to polarization ratios (i.e. the slopes in Fig. 4.3) we derive the 95% confidence intervals, the bounds of which are shown as blue (surface) and green (bottom) dashed lines in Fig. 4.3. A linear color scale is assigned to ratios outside of this two intervals as shown by the inlet in Fig. 4.3.

The same weights (0.16 K of TB_{nn} match 0.0008 of polarization in the minimization) are used for all orthogonal regressions which allows us to compare model regressions with those on the six yearly mean SMOS measurements from 2010 to 2015. By that we estimate which variability in observations can be explained by surface or bottom processes. Again, we use only the ratios between changes in TB_{nn} and polarization to infer their origin and not the absolute values of the measurements.

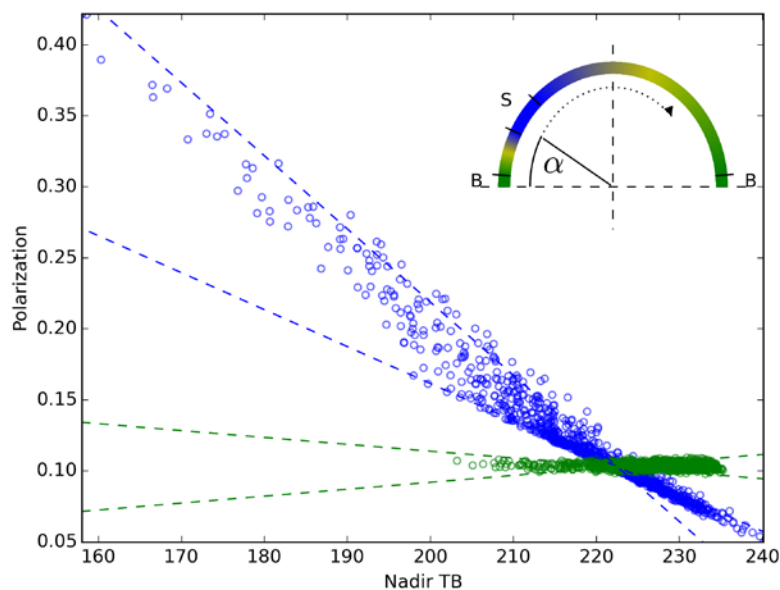


Figure 4.3: Model results (points) varying only near surface parameters (blue) or bottom parameters (green) with 2.5 and 97.5% quantiles (enclosing the 95% confidence interval) of repeated orthogonal regressions on six randomly chosen points (dashed lines). The inlet illustrates the definition of a color scale from the quantiles.

The derived estimate of origin is complemented by an evaluation of the strength of variations. We consider the area from Dome C to Lake Vostoc as predominantly stable, especially compared with ice shelves. In this area (see black frame in central Antarctica in Fig. 4.4) trends of TB_{nn} and polarization are

in the range of $\mp 0.16 \text{ K year}^{-1}$ and $\mp 0.0008 \text{ year}^{-1}$, respectively (not shown). This trends cannot (or only to a small fraction) be attributed to a sensor drift (between -0.03 and $-0.003 \text{ K year}^{-1}$ (Martin-Neira et al., 2016; Mecklenburg et al., 2016) but mostly to variations in the surface state (see case study 4 of this project). Here we take the trends as result of all non melt related natural variability and use their values with units of [K] and [°] as scales for the yearly mean estimates (denoted SC_{TB} and SC_{Pol}).

An alert parameter R_{max} is defined here as $R_{max} = \max(R_i)$; $R_i = \sqrt{\left(\frac{\Delta TB_i}{SC_{TB}}\right)^2 + \left(\frac{\Delta Pol_i}{SC_{Pol}}\right)^2}$, $i \in \{2010, \dots, 2014\}$ with ΔTB_i and ΔPol_i being the year $i+1$ minus year i difference of mean nadir TB and polarization, respectively. In regions with large R_{max} the observed changes are much larger than those of a predominantly stable reference area. To avoid direct observations of surface melt/wet snow we exclude the summer month before deriving the yearly mean. The length of the periods excluded is the same for each year and has been set for each ice shelf individually based on a passive microwave melt detection dataset (see Tab. 4.3, Picard and Fily, 2006).

Table 4.3: Periods used for yearly mean estimates

Ice Shelf / Region	Start Date	End Date
Antarctic Peninsula	Apr. 1st	Aug. 1st
Amery	Mar. 1st	Nov. 1st
Ross	Mar. 1st	Dec. 1st
Ronne Filchner	Feb. 1st	Dec. 1st

4.2.4 Sensitivities

The Sobol sensitivity indices shown in Table 4.4 are derived following method D_1 in Glen and Isaacs (2012). They are based on Monte Carlo simulations ($N=600$, uncertainty based on repeated calculations with $N=200$: <0.05) with the same ranges and distributions for each input parameter as described in Table 4.2 but here without a separation into bottom and surface properties. The first-order or main effect sensitivity index (S_i) represents the sensitivity to changes in one parameter alone but is representative for the used ranges of parameters (instead of e.g. a single model setup which is used as reference). By this approach we can also avoid the assumption of no interactions between parameters which leads to the total effect index (T_i). It is an estimate of the full effect of a parameter, including all interactions with the other parameters. Both, S_i and T_i are calculated for the nadir brightness temperature and the normalized polarization at 40° and are given as parts of the total variance of the runs (184 K^2 and 0.012 for the TB_{nn} and polarization, respectively).

As S_i neglects all interactions between input parameters and T_i includes the influence of interactions with all other parameters, it is expected that the sum of all S_i (T_i) is below (above) 1 while the difference

of the two is a measure of the importance of interactions. But how to convert Sobol indices to the absolute influence of a parameter on the signal? As an Example: the marine ice concentration is varied from 0 to 100% (with an equal distribution) and the main-effect and total effect indices for the nadir TB are 0.09 and 0.11 respectively. The total variance in TB is 184 K² from which about 10% (18 K²) can be attributed to marine ice.

Table 4.4: Sobol sensitivity indices

	Bottom				Surface			∅
	T(z)	H	c_{MI}	c_{RI}	ζ	a_σ	ρ_s	
$S_i(TB_{nn})$	0.02	0.05	0.09	0.01	0.15	0.28	0.34	0.94
$T_i(TB_{nn})$	0.03	0.07	0.11	0.01	0.19	0.33	0.40	1.14
$S_i(Pol)$	0.00	0.00	0.00	0.00	0.10	0.18	0.58	0.86
$T_i(Pol)$	0.00	0.00	0.00	0.00	0.16	0.24	0.69	1.09

Table 4.4 shows that the sensitivities of both, TB_{nn} and the polarization are substantially higher to surface properties than to bottom properties. This finding is clearly dependent on the used parameter ranges but illustrates that a retrieval of individual bottom properties strongly impeded by a relative large superimposed signal from not well known surface properties of ice shelves. This is however not necessarily the case in regions where the influence on the signal from surface properties is smaller and less variable (like in central Antarctica).

Our approach is based on the different ratios of influencing TB_{nn} and the polarization of the two sets of parameters. And in fact, $\frac{S_i(TB_{nn})}{S_i(Pol)}$ and $\frac{T_i(TB_{nn})}{T_i(Pol)}$ are more than one order of magnitude larger for each bottom parameter than for surface parameters (not including c_{RI} here, which has a very small influence in general).

4.2.5 A brief Overview

The general picture of the product is as expected: while there are areas of surface and bottom driven variability at ice shelves, surface processes are dominating inland (Fig. 4.4), however there are grounded areas with detected bottom changes, e.g. at the Antarctic Peninsula (see Product Validation Report for a closer look).

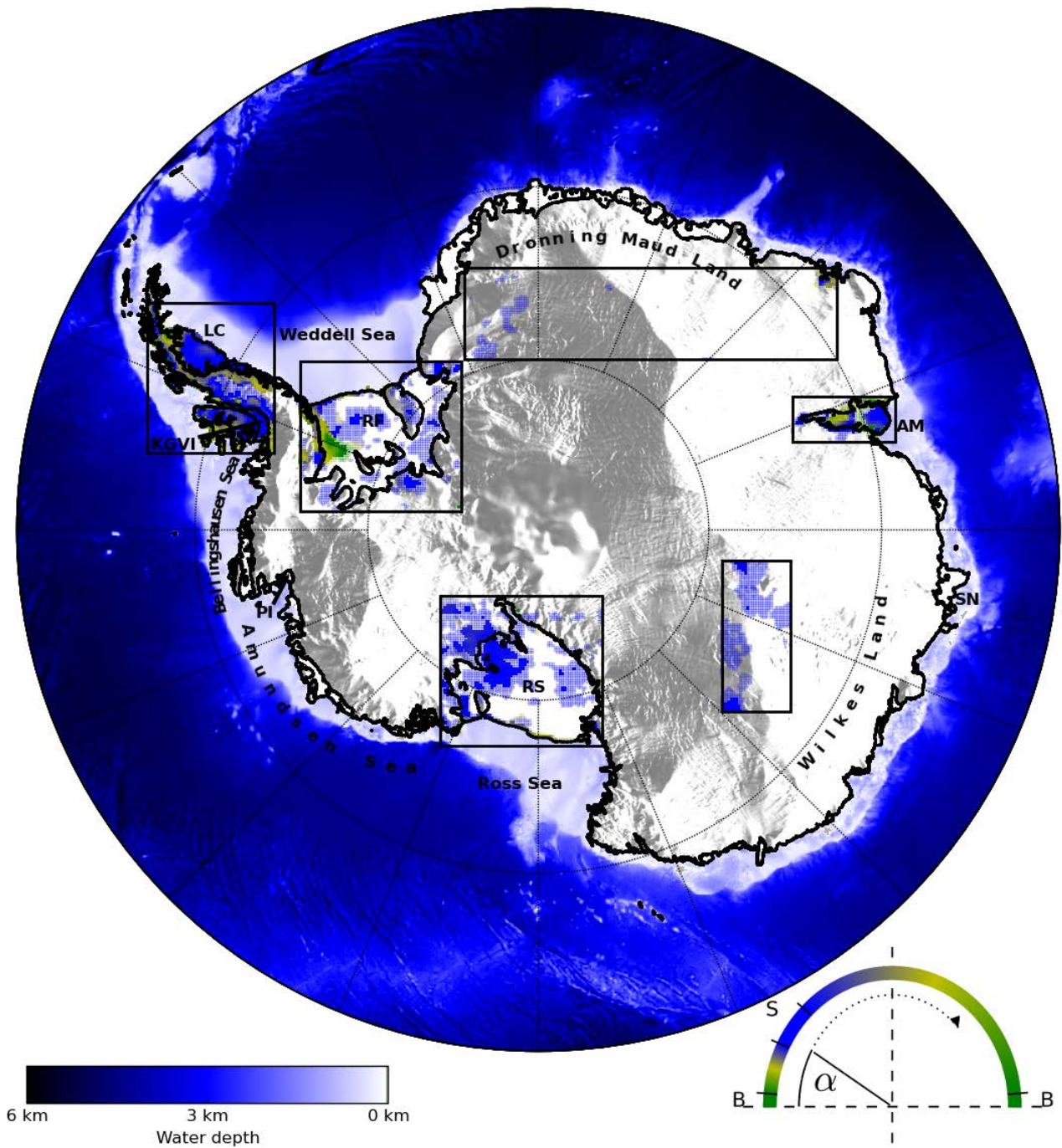


Figure 4.4: Locations of six study regions (frames) with estimates of the origin of SMOS variations for $R_{max} > 6$ (pale colors) and $R_{max} > 10$ (intense colors). Grounding and coast lines (black) from MODIS Mosaik of Antarctica 2009 as well as surface (shades) and sea floor topography from Bedmap-2.

5 Case study n.4: characterization of surface processes

(LGGE in cooperation with IFAC, CESBIO)

5.1 Brief description of the case study

The state of the surface is essential to understanding and predicting the surface energy and mass budgets, which are two key nivo-meteorological variables of interest for the study of the climate and as a contribution to the sea level of ice-sheets. Snow properties such as grain size, wetness, density, and roughness are linked to air temperature, surface wind, precipitations, etc., which are important in helping climate models to retrieve surface processes and to monitor climate change.

SMOS observations could help to detect fresh snow in order to supply information about precipitations, to follow variations in roughness linked to wind, as well as monitor melting periods (number of melting days per year, duration, starting date, etc.). Thanks its large penetration depth, SMOS observations could detect whether melt is deep and impacts on snowpack stability, contrary to higher microwave frequencies, which are sensitive to the first meters of snowpack.

A first preview of SMOS observations has shown that two main regions can be identified and have been explored separately (see Figure 4 in [RD.3]). One, in the internal part of the continent, is a region in which the ice sheet is always dry. The L-band brightness temperature is very stable, and any small variations observed could be interpreted as changes in the surface state. A detailed analyse have been performed at the Dome C test site. A clear sensitivity of brightness temperature at horizontal polarization to surface state have been highlighted thank to the numerous in situ measurements and the WALOMIS snow emission model (Leduc-Leballeur et al., in prep.). Surface snow density and thickness of surface layer have been identified as key parameter to explain the temporal variations observed at Dome C. However, further work needs to explore in more details this sensitivity and the extension of this study to the whole dry snow is an avenue but could be challenging because of the lack of in situ measurements

The second region is the wet snow area, which is located mainly along the coast and on ice-shelves. Here, the surface state is affected by seasonal melting events that considerably influence the snowpack. Indeed, the episodic presence of liquid water forms a refrozen snow layer and leads to a sustained decrease in the L-band brightness temperature observation after the melt season as compared to before the melt season. Moreover, annual snow accumulation is greater than in dry snow region. For these reasons, surface processes along the coast and ice-shelves are expected to be different from the internal ice-sheet. Thus, SMOS observations in this region could help to follow and characterize surface melting events.

5.2 Characterization of surface processes: Retrieval Approach or Methodology – Final ATBD

Remote sensing by passive and active microwaves is sensitive to surface melting. Indeed, the onset of melting produces a marked rise of brightness temperature that is caused by moisture in the near-surface firn due to the large difference between the dielectric constants of ice and water in the microwave domain. Several efficient algorithms have been developed to detect these dielectric changes in Greenland (e.g. Abdalati & Steffen, 1997) and in Antarctica (e.g. Ridley, 1993; Zwally & Fiegles, 1994; Torinesi et al., 2003). We have exploited these studies in order to set up an algorithm for the detection of the melt in Antarctica from L-band SMOS observations.

5.2.1 SMOS observation selection process

The melting product is estimated from the SMOS Level 3 product. The RE04 reprocessed version distributed by CATDS (Centre Aval de Traitement des Données SMOS; <http://www.catds.fr/>) was used from July 2010 to June 2015. The product is geolocated on an Equal-Area Scalable Earth version 2.0 grid (EASE-Grid2; Brodzik et al., 2012), with an oversampled resolution of about 628 km², which is distorted in the polar regions (around 100 x 6 km² as latitude x longitude; Kerr et al., 2013). The daily-averaged brightness temperature at 52.5° of incidence angle was used.

Time-series in each point have been smoothed by the way of a moving mean with a 7-day window. This allows removing on one hand, the radiometric noise and on the other hand the short gaps in time-series. For gaps of duration less than 4 days, the missing brightness temperatures are filling by the moving mean. For gaps equal or longer than 4 days, the brightness temperatures stay missing at this date. Years with more than two month of missing brightness temperatures are simply ignored.

A mask is used to Mask used to exclude the ocean, the mixing land/ocean pixels as well as areas never experiencing melting. This mask is already used in a similar product of melting detection by microwave satellite (Picard et al., 2006).

5.2.2 The algorithm

Although the emissivities of wet firn at horizontal and vertical polarizations are nearly equal, the emissivity of dry firn at horizontal polarization is significantly lower than at vertical polarization. Therefore, horizontal polarization is used, because the increase in brightness temperature with melting is larger at horizontal than at vertical polarization.

Zwally et al. (1994) and Torinesi et al. (2003) suggested a criterion to detect melting day from 19 GHz brightness temperature. Melt induces large increases of brightness temperature and an annually and regionally varying threshold can be calculated. All values of brightness temperature above the annual mean plus this threshold are associated with melting. This threshold is proportional to the standard deviation of the signal in order to take into account the spatial variability of its amplitude.

Thus, the threshold T above which a brightness temperature value is considered to be a melt signal is the mean M plus N standard deviations σ :

$$T = M + N\sigma \quad (5.1)$$

For each year from 2010 to 2015, the annual mean of brightness temperature at horizontal polarization is calculated between 1 July and 31 June in each grid point. This annual mean allow to take into account the interannual variability of the signal. But, it is also essential to remove the bias introduces by the high values typical of melting, which do not reflect average values of unaffected period. Thus, these melting events are filtered out by eliminating values more than 10 K above the annual mean. This process is repeated two times. The first time, the mean is calculated using all the values (without any filter); then strong melt signals are filtered out and the calculation is performed a second time. Thus M and σ are calculated from the obtained time-series vary for each year and each grid point.

The value of N is a constant and the selected value is $N = 2.5$ (Torinesi et al., 2003; Picard et al., 2006). This optimal value is determined by an analyse based on daily air surface temperature (Torinesi et al., 2003). N had been adjusted to detect all and only the real melting days, as possible. The N is chosen so that most melt events correspond to daily maximum temperatures above -5°C .

5.2.3 Final product

The algorithm is designed to detect individual melting events for every grid points and each day. It returns two possible values: 1 for the status melted, or 0 for not-melted. Figure 5-1 shows an example of melting detection from 2010 and 2016 in the East of Antarctic close to the Amery ice-shelf. The threshold separately defined for each year (black lines) allows a good detection of the main seasonal peak of brightness temperature.

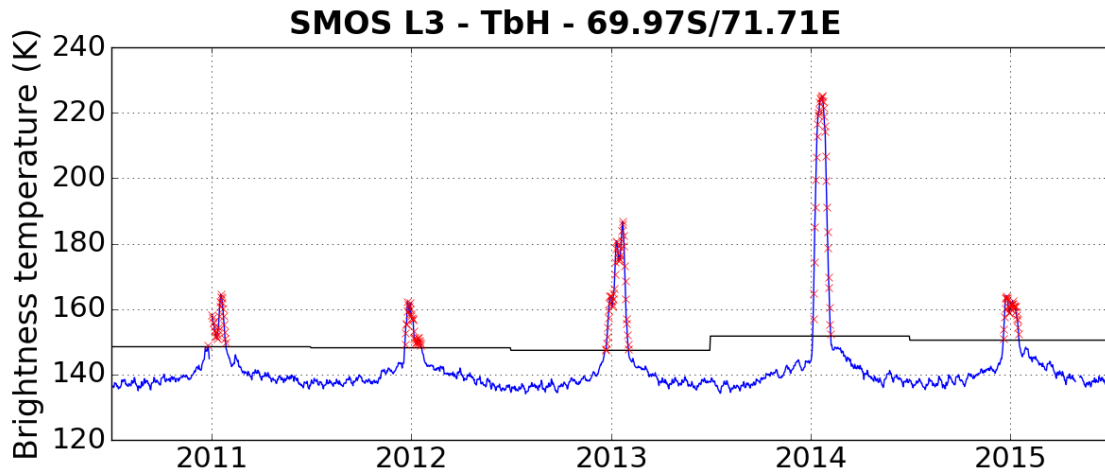


Figure 5-1: Brightness temperature at horizontal polarization (K, blue) from SMOS at 68°S, 71.7°E from July 2010 to June 2015. Threshold defined by the algorithm is represents in black and the detected melting days are in red stars.

Figure 5-2 give an example of number of melting days detected by SMOS through the algorithm for the 2013-2014 year. Melt is concentrate along the coast with some maximum in the ice-shelves area. The reliability of the algorithm and this final product will be discussed in the Product Validation Report (D6).

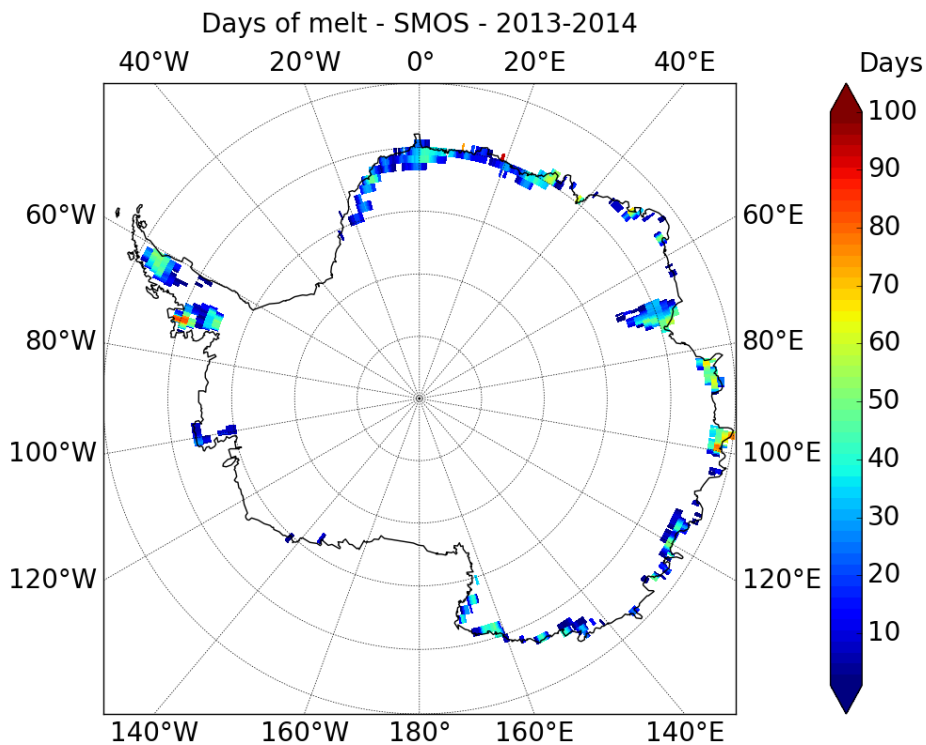


Figure 5-2: Number of melting days detected by algorithm from SMOS brightness temperature for the 2013-2014 year.

6 References

- Abdalati, W., & Steffen, K., 1997, Snowmelt on the Greenland ice sheet as derived from passive microwave satellite data. *Journal of Climate*, 10, 165–175.
- Agosta, C., Favier, V., Krinner, G., Gallée, H., Fettweis, X., & Genthon, C. (2013). High-resolution modelling of the Antarctic surface mass balance, application for the twentieth, twenty first and twenty second centuries. *Climate dynamics*, 41(11-12), 3247-3260.
- Alley, R., Bolzan, J., & Whillans, I. (1982). Polar firn densification and grain growth. *Ann. Glaciol.*, 3, 7–11.
- Augustin L., et al. (2004). Eight glacial cycles from an Antarctic ice core. *Nature*, 429, 623-628, doi:10.1038/nature02599
- Bamber J. L., D. G. Vaughan, I. Joughin, “Widespread Complex Flow in the Interior of the Antarctic Ice Sheet”, *SCIENCE*, 18 Feb 2000, pp. 1248-1250
- Bereiter, B., Fischer, H., Schwander, J., & Stocker, T. F. (2014). Diffusive equilibration of N₂, O₂ and CO₂ mixing ratios in a 1.5 million years old ice core. *The Cryosphere*, 8(1), 245-256.
- Bevington, Philip R., Robinson, D. Keith. (2003) *Data reduction and error analysis for the physical sciences* - Boston : McGraw-Hill.
- Brodzik, M. J., Billingsley, B., Haran, T., Raup, B., & Savoie, M. H. (2012). Ease-grid 2.0: Incremental but significant improvements for earth-gridded data sets. *ISPRS International Journal of Geo-Information*, 1, 32{45. doi:10.3390/ijgi1010032.
- Brogioni, M., Macelloni, G., Montomoli, F., & Jezek, K.C., (2015). Simulating Multifrequency Ground-Based Radiometric Measurements at Dome C—Antarctica. *Selected Topics in Applied Earth Observations and Remote Sensing, IEEE Journal of* , PP-99, 1-13, 10.1109/JSTARS.2015.2427512
- Burke, W. J., Schmugge, T., & Paris, J. F. (1979). Comparison of 2.8-and 21-cm microwave radiometer observations over soils with emission model calculations. *Journal of Geophysical Research: Oceans* (1978–2012), 84(C1), 287-294.
- Brucker L., Dinnat E.P., Picard G., Champollion N., “Effect of Snow Surface Metamorphism on Aquarius L-Band Radiometer Observations at Dome C, Antarctica” , *IEEE Transactions on Geoscience and Remote Sensing*, 52(11): 1-10, doi: 10.1109/TGRS.2014.2312102 , 2014a

Brucker L., Dinnat E. P., Koenig L. S., “Weekly gridded Aquarius L-band radiometer/scatterometer observations and salinity retrievals over the polar regions – Part 2: Initial product analysis”, *The Cryosphere*, 8:915-930, www.the-cryosphere.net/8/915/2014, doi:10.5194/tc-8-915-2014, 2014b

Dee, D. P., Uppala, S. M., Simmons, A. J., Berrisford, P., Poli, P., Kobayashi, S., ... & Bechtold, P. (2011). The ERA-Interim reanalysis: Configuration and performance of the data assimilation system. *Quarterly Journal of the Royal Meteorological Society*, 137(656), 553-597.

Drinkwater, M. R., N. Floury, M. Tedesco, “L-band ice-sheet brightness temperatures at Dome C, Antarctica: Spectral emission modeling, temporal stability and impact of the ionosphere”, *Annals of Glaciology*, 39, 2003.

Fox Maule, C., Purucker, M. E., Olsen, N., & Mosegaard, K. (2005). Heat flux anomalies in Antarctica revealed by satellite magnetic data. *Science*, 309(5733), 464-467.

Fretwell, P., Pritchard, H. D., Vaughan, D. G., Bamber, J. L., Barrand, N. E., Bell, R., Bianchi, C., Bingham, R. G., Blankenship, D. D., Casassa, G., Catania, G., Callens, D., Conway, H., Cook, A. J., Corr, H. F. J., Damaske, D., Damm, V., Ferraccioli, F., Forsberg, R., Fujita, S., Gim, Y., Gogineni, P., Griggs, J. A., Hindmarsh, R. C. A., Holmlund, P., Holt, J. W., Jacobel, R. W., Jenkins, A., Jokat, W., Jordan, T., King, E. C., Kohler, J., Krabill, W., Riger-Kusk, M., Langley, K. A., Leitchenkov, G., Leuschen, C., Luyendyk, B. P., Matsuoka, K., Mouginot, J., Nitsche, F. O., Nogi, Y., Nost, O. A., Popov, S. V., Rignot, E., Rippin, D. M., Rivera, A., Roberts, J., Ross, N., Siegert, M. J., Smith, A. M., Steinhage, D., Studinger, M., Sun, B., Tinto, Welch B. K., B. C., Wilson, D., Young, D. A., Xiangbin, C., and Zirizzotti, A. (2013). Bedmap2: improved ice bed, surface and thickness datasets for Antarctica. *The Cryosphere*, 7, 375-393, doi:10.5194/tc-7-375-2013

Fréville, H., Brun, E., Picard, G., Tatarinova, N., Arnaud, L., Lanconelli, C., & Van Den Broeke, M. (2014). Using MODIS land surface temperatures and the Crocus snow model to understand the warm bias of ERA-Interim reanalyses at the surface in Antarctica. *The Cryosphere*, 8(4), 1361-1373.

Hall, D. K., Key, J. R., Casey, K., Riggs, G., & Cavalieri, D. J. (2004). Sea ice surface temperature product from MODIS. *Geoscience and Remote Sensing, IEEE Transactions on*, 42(5), 1076-1087.

Herron, M. M., & Langway Jr, C. C. (1980). Firn densification: an empirical model. *Journal of Glaciology*, 25, 373-385.

Hörhold, M. W., Kipfstuhl, S., Wilhelms, F., Freitag, J., & Frenzel, A. (2011). The densification of layered polar firn. *Journal of Geophysical Research: Earth Surface* (2003–2012), 116(F1).

Jezeq, K. C., J. T. Johnson, M. R. Drinkwater, G. Macelloni, L. Tsang, M. Aksoy, and M. Durand (2015): "Radiometric Approach for Estimating Relative Changes in Intraglacier Average Temperature" IEEE Trans. on Geoscience and Remote Sensing, Vol. 53, No. 1, pp 134-143.

Kaleschke, L., Maaß, N., Haas, C., Hendricks, S., Heygster, G., & Tonboe, R. T. (2010). A sea-ice thickness retrieval model for 1.4 GHz radiometry and application to airborne measurements over low salinity sea-ice. *The Cryosphere*, 4(4), 583-592.

Kerr, Y. H., Jacqueline, E., Al Bitar, A., Cabot, F., Mialon, A., Richaume, P., Quesney, A., & Berthon, L. (2013). CATDS SMOS L3 soil moisture retrieval processor { Algorithm Theoretical Baseline Document (ATBD). Technical Report SO435 TN-CBSA-GS-0029, Issue 2.e. URL: http://www.cesbio.upstlse.fr/SMOS_blog/wp-content/uploads/2013/08/ATBD_L3_436_rev2_draft.pdf.

Klein, L., & Swift, C. T. (1977). An improved model for the dielectric constant of sea water at microwave frequencies. *Antennas and Propagation, IEEE Transactions on*, 25(1), 104-111.

Kristensen, S. S., S.S. Søbjaerg, J. E. Balling and N. Skou (2013): "DOMECair Campaign, EMIRAD Data: Presentation and Analysis" DTU Space report, 12/11 – 2013, 118 p.

Lambrecht, A., Sandhager, H., Vaughan, D. G., & Mayer, C. (2007). New ice thickness maps of Filchner–Ronne Ice Shelf, Antarctica, with specific focus on grounding lines and marine ice. *Antarctic Science*, 19(04), 521-532.

Le Brocq, A. M., A.J. Payne, and A. Vieli, "An improved Antarctic dataset for high resolution Geography numerical ice sheet models (ALBMAP v1)", *Earth Syst. Sci. Data*, 2, 247-260, www.earth-syst-sci-data.net/2/247/2010/, doi:10.5194/essd-2-247-2010.

Leduc-Leballeur, M., Picard, G., Mialon, A., Arnaud, L., Lefebvre, E., Possenti, P., & Kerr, Y. (2015). Modeling L-Band Brightness Temperature at Dome C in Antarctica and Comparison With SMOS Observations. *Geoscience and Remote Sensing, IEEE Transactions on*, 53(7), 4022-4032.

Maaß, N., Kaleschke, L., Tian-Kunze, X., and Drusch, M.: Snow thickness retrieval over thick Arctic sea ice using SMOS satellite data, *The Cryosphere*, 7, 1971–1989, 2013.

Macelloni, G., M. Brogioni, P. Pampaloni, A. Cagnati, and M. R. Drinkwater, "DOMEX 2004: An Experimental Campaign at Dome-C Antarctica for the Calibration of Spaceborne Low-Frequency Microwave Radiometers", *IEEE Trans. on Geoscience and Remote Sensing*, Vol. 44, No. 10, pp 2642-2653, 2006.

Macelloni, G., M. Brogioni, S. Pettinato, F. Montomoli, F. Monti, and T. Casal, "L-band Characterization of Dome-C Region using Ground and Satellite Data", *Proc.IGARSS'13*, pp. 3427-3440, 2013.

Macelloni, G., M. Brogioni, S. Pettinato, R. Zasso, A. Crepaz, J. Zaccaria, B. Padovan, and M. Drinkwater (2013): "Ground-Based L-Band Emission Measurements at Dome-C Antarctica: The DOMEX-2 Experiment" *IEEE Trans. on Geoscience and Remote Sensing*, Vol. 51, No. 9, pp 4718-4730.

Macelloni G., M. Leduc-Leballeur, M. Brogioni, C. Ritz, G. Picard, "Analyzing and modeling the SMOS spatial variations in the East Antarctic Plateau", *Remote Sensing of Environment*, Volume 180, July 2016, Pages 193-204, ISSN 0034-4257, <http://dx.doi.org/10.1016/j.rse.2016.02.037>.

Martin-Neira, M., Oliva, R., Corbella, I., Torres, F., Duffo, N., Duran, I., Kainulainen, J., Closa, J., Zurita, A., Cabot, F., et al.: SMOS instrument performance and calibration after six years in orbit, *Remote Sensing of Environment*, 180, 19–39, 2016.

Mätzler C. (2006). *Thermal Microwave Radiation: Applications for Remote Sensing Chapter 5, Microwave dielectric properties of ice*. Eds.

Mätzler, C. (2001): "Application of SMOS over Terrestrial Ice and Snow" 3rd SMOS Workshop, DLR, Germany, December 10-12, 9p.

Mecklenburg, S.; Drusch, M.; Kerr, Y.H.; Font, J.; Martin-Neira, M.; Delwart, S.; Buenadicha, G.; Reul, N.; Daganzo-Eusebio, E.; Oliva, R.; Crapolicchio, R., (2012), *ESA's Soil Moisture and Ocean Salinity Mission: Mission Performance and Operations, Geoscience and Remote Sensing, IEEE Transactions on* , vol.50, no.5, 1354,1366, 2012, doi: 10.1109/TGRS.2012.2187666

Mecklenburg, S., Drusch, M., Kaleschke, L., Rodriguez-Fernandez, N., Reul, N., Kerr, Y., Font, J., Martin-Neira, M., Oliva, R., Daganzo-Eusebio, E., et al.: *ESA's Soil Moisture and Ocean Salinity mission: From science to operational applications, Remote Sensing of Environment*, 180, 3–18, 2016.

Pablos, M., Piles, M., González-Gambau, V., Camps, A., & Vall-Ilossera, M. (2014). Ice thickness effects on Aquarius brightness temperatures over Antarctica. *J. Geophys. Res. Oceans*, 120, 2856–2868, 10.1002/2014JC010151. Parrenin F, G. Dreyfus, G. Durand, S. Fujita, O. Gagliardini, F. Gillet, J. Jouzel, K. Kawamura, N. Lhomme, V. Masson-Delmotte, C. Ritz, J. Schwander, H. Shoji, R. Uemura, O. Watanabe, N. Yoshida. (2007). 1-D-Ice flow modelling at EPICA Dome C and Dome Fuji, East Antarctica, *Climate of the Past*, 3, 243- 259.

Peng, J., Kim, E., & Piepmeier, J. (2013). Global Simplified Atmospheric Radiative Transfer Model at L-Band. *Geoscience and Remote Sensing Letters, IEEE*, 10(3), 437-440.

Picard, G., Brucker, L., Roy, A., Dupont, F., Fily, M., & Royer, A. (2013). Simulation of the microwave emission of multi-layered snowpacks using the dense media radiative transfer theory: the DMRT-ML model. *Geoscientific Model Development*, 6, 1061-1078

Picard G., Fily M., 2006, Surface melting observations in Antarctica by microwave radiometers: correcting 26 year-long timeseries from changes in acquisition hours. *Remote Sensing of Environment*.

Ridley, J., 1993, Surface melting on Antarctic Peninsula ice shelves detected by passive microwave sensors. *Geophysical Research Letters*, 20(23), 2639–2642.

Ritz, C. (1989). Interpretation of the temperature profile measured at Vostok, East Antarctica. *Annals of Glaciology*, 12, 138–144.

Robin, G. D. Q. (1955). Ice movement and temperature distribution in glaciers and ice sheets. *Journal of Glaciology*, 2(18), 523-532.

Salamatin, A.N., Lipenkov, V.Ya., Barnola, J.-M., Hori, A., Duval, P., & Hondoh, T. (2009). Snow/Firn densification in polar ice sheets. In *Hondoh, T. ed. Physics of ice core records v. 2*. Sapporo, Hokkaido University Press, 195–222

Shapiro, N. M., & Ritzwoller, M. H. (2004). Inferring surface heat flux distributions guided by a global seismic model: particular application to Antarctica. *Earth and Planetary Science Letters*, 223(1), 213-224.

Skou, N., S. S. Kristensen, , S. S. Søbjaerg, and J. Balling (2013): “DOMEair: An Airborne Campaign in Antarctica Supporting SMOS Calibration” Proceedings ESA Living Planet Symposium, Edinburgh, September 2013, 8p.

Skou, N., S. S. Kristensen, S. S. Søbjaerg, and J. Balling, “Mapping of the Dome-C Area in Antarctica by an Airborne L-band Radiometer”, Proceedings of IGARSS 2014, July 2014, pp 3610 – 3613.

Skou, N., S. S. Søbjaerg, J. Balling, S. S. Kristensen, “A Second Generation L-band Digital Radiometer for Sea Salinity Campaigns”, Proc. IGARSS'06, pp. 3984-3987, 2006.

Søbjaerg, S. S., S. S. Kristensen, J. Balling, N. Skou, “The Airborne EMIRAD L-band Radiometer System”, Proc. IGARSS'13, pp. 1900-1903, 2013.

Torinesi O., Fily M., and Genthon C., 2003, Interannual variability and trend of the Antarctic summer melting period from 20 years of spaceborne microwave data, *J. of Climate*, 16(7), 1047-1060.

Tiuri, Martti E., Sihvola, A.H., Nyfors, E., Hallikaiken, M. (1984). The complex dielectric constant of snow at microwave frequencies. *Oceanic Engineering, IEEE Journal of*, 9-5, 377-382, 10.1109/JOE.1984.1145645

Ulaby, F. T., Long, D. G., Blackwell, W. J., Elachi, C., Fung, A. K., Ruf, C., Sarabandi, K., Zebker, H. A., and Van Zyl, J.: *Microwave radar and radiometric remote sensing*, University of Michigan Press Ann Arbor, 2014.

Van der Veen, C. J., "Fundamentals of Glacier Dynamics". Rotterdam, The Netherlands: A. A. Balkema, 1999.

Van Liefferinge, B. V., & Pattyn, F. (2013). Using ice-flow models to evaluate potential sites of million year-old ice in Antarctica. *Climate of the Past*, 9(5), 2335-2345.

Vionnet, V., Brun, E., Morin, S., Boone, A., Faroux, S., Le Moigne, P., ... & Willemet, J. M. (2012). The detailed snowpack scheme Crocus and its implementation in SURFEX v7. 2. *Geoscientific Model Development*, 5, 773-791.

West, R. D., Winebrenner, D. P., Tsang, L., & Rott, H. (1996). Microwave emission from density-stratified Antarctic firn at 6 cm wavelength. *J. Glaciol.*, 42-140, 63 -76

Zhao, T., Shi, J., Bindlish, R., Jackson, T. J., Kerr, Y. H., Cosh, M. H., Cui, Q., Li, Y., Xiong, C., and Che, T.: Refinement of SMOS multiangular brightness temperature toward soil moisture retrieval and its analysis over reference targets, *IEEE Journal of Selected Topics in Applied Earth Observations and Remote Sensing*, 8, 589–603, 2015.

Zwally H. (1977). Microwave emissivity and accumulation rate of polar firn. *J. Glaciol.*, 18-79, 195–215.

Zwally, H. J., Fiegles, S., 1994, Extent and duration of Antarctic surface 829 melting. *Journal of Glaciology*, 40(136), 463.